Monte Carlo analysis of semiconductor devices: The DAMOCLES program

by S. E. Laux M. V. Fischetti D. J. Frank

The behavior of small semiconductor devices is simulated using an advanced Monte Carlo carrier transport model. The model improves upon the state of the art by including the full band structure of the semiconductor, by using scattering rates computed consistently with the band structure, and by accounting for both longand short-range interactions between carriers. It is sufficiently flexible to describe both unipolar and bipolar device operation, for a variety of semiconductor materials and device structures. Various results obtained with the associated DAMOCLES program for n- and p-channel Si MOSFETs, GaAs MESFETs, and Si bipolar junction transistors are presented.

[®]Copyright 1990 by International Business Machines Corporation. Copying in printed form for private use is permitted without payment of royalty provided that (1) each reproduction is done without alteration and (2) the *Journal* reference and IBM copyright notice are included on the first page. The title and abstract, but no other portions, of this paper may be copied or distributed royalty free without further permission by computer-based and other information-service systems. Permission to *republish* any other portion of this paper must be obtained from the Editor.

1. Introduction

The simulation of the behavior of semiconductor device structures obtained by solving transport equations has proven to be important in device design. Since its inception in the late 1960s and early 1970s [1-7], numerical device simulation has been governed by two important trends, driven by progress in integrated electronics itself. First, miniaturization has resulted in device structures which are increasingly sensitive to geometric parameters. Devices which once could be adequately described by a one-dimensional model have become the exception rather than the rule: Two- and three-dimensional models have accordingly grown in importance. Secondly, as a by-product of miniaturization, the appropriateness of the physical basis normally incorporated into device-modeling programs continues to erode. The distance scale within a typical device can now approach the distance between scattering events in the crystal; this introduces nonequilibrium transport effects which a "drift-diffusion" formulation [8, 9] does not include [10, 11].

Increasing either the geometric dimensionality or the physical rigor of a device model comes at the expense of

increased computing times. At present, full three-dimensional calculations embrace conventional drift-diffusion physics; the use of more rigorous methods is at present confined to two-dimensional treatments. Historically, the need to address geometric dependencies proved more urgent, so three-dimensional, drift-diffusion device models are relatively mature today [12, 13]. The FIELDAY program, as described in 1981 [14], typifies such an effort and is still in use today. The recent availability of a three-dimensional program dedicated to MOSFET simulation in the public domain underscores this maturity [15]. In contrast, device modeling which attempts to move beyond drift-diffusion analysis is less established.

Both deterministic [16–33] and stochastic [34–59] approaches to incorporating a more complete solution to the Boltzmann transport equation (BTE) for device modeling have been demonstrated; this will remain a fertile research topic for some years to come. This paper revisits the topic of numerical device modeling as described by Buturla et al. [14], but with an emphasis on results obtained after including more of the physics relevant to modeling exploratory device structures. Our device modeling program is called DAMOCLES, an acronym for Device Analysis using Monte Carlo et Poisson solver [60].

The DAMOCLES program can be used to solve the three-dimensional Boltzmann transport equation using a Monte Carlo technique self-consistently with the Poisson equation for a two-dimensional device cross section. The carrier transport model describes both electron and/or hole motion, and improves upon the state of the art by including the full band structure of the semiconductor, by using scattering rates computed consistently with the band structure, and by accounting for both long- and short-range interactions between carriers. Specialized statistical sampling techniques are employed to obtain accurate information on rare events, i.e., in regions of low carrier density and/or extreme carrier heating. The program is sufficiently flexible to permit the simulation of rather general device structures with realistic doping profiles. Use of a dedicated, interactive graphics facility permits the rapid interpretation of model results, which may be viewed without interrupting an analysis in progress.

Although the DAMOCLES program has been described recently in some detail [61–63], Section 2 of this paper summarizes recent enhancements and extensions. What began as a Monte Carlo treatment for unipolar electron transport only in a self-consistent electric field has now been extended to include unipolar hole transport or bipolar transport. This greatly expands the number of device structures which can be simulated with DAMOCLES. An additional improvement which

implements a more accurate relationship among carrier density, temperature, Fermi energy, and average energy is also detailed. This improvement is needed to handle degenerate conditions, and makes screening lengths and energies more accurate in heavily doped regions. The implementation of a method to improve statistics for rare events has been refined and is also described. In Section 3 new results obtained for submicron silicon MOSFETs, both n- and p-channel and at 300 and 77 K, are given. Section 4 describes results for n-channel GaAs MESFETs, and Section 5 demonstrates the bipolar simulation capability for idealized npn and pnp device structures. Taken together, the ability to model these disparate device structures, in the context of a state-ofthe-art physical basis, underscores the flexibility and power of our approach. Section 6 offers conclusions and directions for future work.

2. Recent enhancements to the model

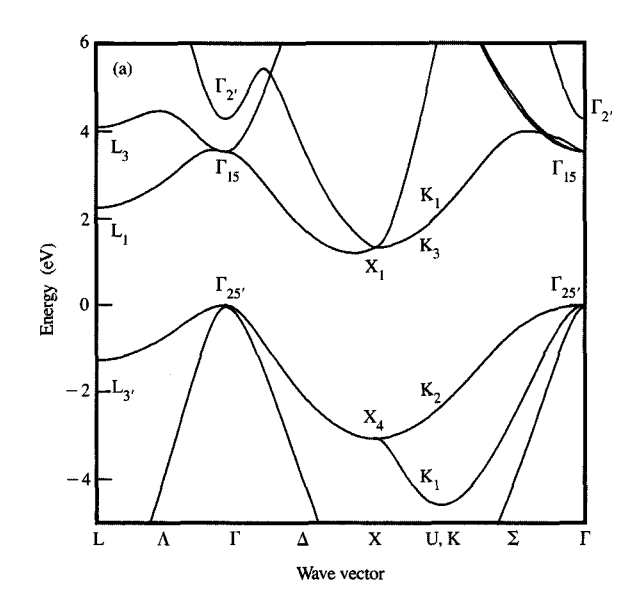
The physical phenomena underlying the DAMOCLES program have recently been described [61]. However, the following improvements and enhancements to the program have since been made:

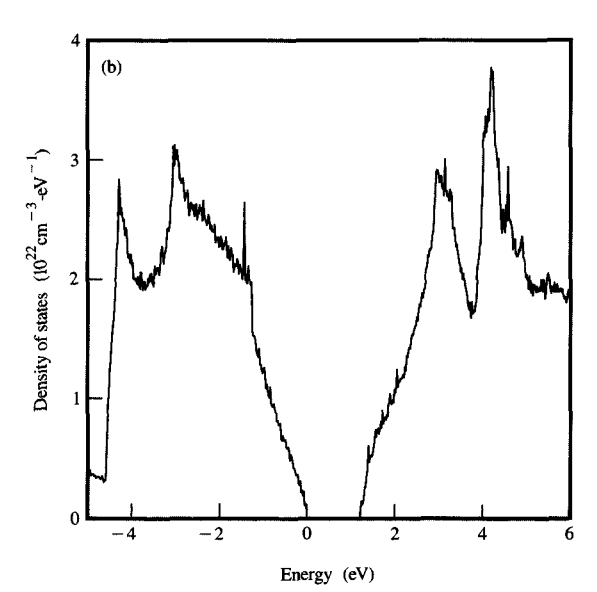
- A Monte Carlo treatment of hole transport is now included in the model.
- A more accurate relationship among carrier density, temperature, Fermi energy, and average energy under degenerate conditions has been implemented.
- Improvements in gathering statistics on rare events associated with low carrier densities and/or energetic carriers have been made.

These are discussed in turn.

♦ Hole transport

The incorporation of holes into the DAMOCLES program is conceptually simple and is analogous to the procedure used to implement and calibrate electron transport. For clarity, this discussion is limited to holes in silicon. First, empirical pseudopotentials [64] are used to generate the valence band structure for holes. The band structure and density of states (DOS) obtained are shown in Figure 1. The band structure is even more complicated than for electrons, due to the warping and strong nonparabolicity of the bands. Note the explicit presence of the heavy- and light-hole bands, as well as the split-off band, in the model. Since local pseudopotentials without spin-orbit interaction are employed, one of the doubly degenerate light-hole bands is shifted by the known spinorbit interaction energy of 0.045 eV. This is a satisfactory approximation for crystals with small spin-orbit coupling, such as silicon. The calibration of deformation potentials is done by fitting bulk experimental data. After fitting





Elama.

(a) Silicon band structure and (b) density of states for electrons and holes. Each was obtained from empirical pseudopotential calculations. The split-off valence band can be seen at the right edge of (a) along the Σ -line. The nomenclature indicated in (a) is in standard use in band-structure calculations [64]. From [63], reproduced with permission.

drift velocity versus electric field curves [65] and impact ionization coefficients [66, 67], the parameters we employ [63] are $\Delta_{\rm ac} = 3.5 \text{ eV}$, $(\Delta K)_{\rm op} = 6.0 \times 10^8 \text{ V/cm}$, $E_{\rm th} = 1.21 \text{ eV}$, $P/\tau_{\rm op}(E_{\rm th}) = 9.0 \times 10^{14} \text{ s}^{-1}$ (respectively, the acoustic phonon deformation potential, the optical

phonon deformation potential, the threshold energy for impact ionization, and the prefactor in the Keldysh formula for impact ionization). In Figure 2, the electric field dependence of the hole drift velocity and average energy is shown and compared to experimental data, at 77 and 300 K. For all device simulations in this paper, it is assumed that use is made of (100) material.

Internal to DAMOCLES, information for all particles (e.g., position, energy, wave vector) is collated in an unordered fashion, with a single "type" array identifying the particle as an electron or hole. This permits the previous vectorized treatment of short-range particle interaction [61] to carry over directly to electronelectron, electron-hole, and hole-hole scattering in the bipolar case. Carrier kinetic energies are always positive and relative to the local conduction/valence band edge minimum. This permits the previous electron-only integration of the equations of motion to be readily extended to the bipolar case as well. In contrast to the electron implementation, no analogue to the mixture of analytic and numeric bands (below and above a kinetic energy threshold, respectively) exists for holes. The valence band structure is not amenable to this approach, given its complicated shape. Therefore, numeric bands are employed exclusively for holes.

• Tabulation of integrals involving density of states
The relationship yielding carrier density and average
energy given the Fermi energy and temperature involves
Fermi-Dirac integrals of order 1/2 and 3/2, respectively,
assuming parabolic energy bands [68]. Until now, such
expressions were used in DAMOCLES with a carrier
effective mass derived from the full energy band
structure. This approach errs under the condition of
degeneracy, which occurs for high carrier concentrations
or low temperatures. In general, a more rigorous
treatment is required. The discussion is given for
electrons, but is easily transposed for holes.

The electron density n with Fermi energy $E_{\rm Fn}$ and temperature $T_{\rm n}$ is given by an integral over the conduction band,

$$n(E_{\rm Fn}, T_{\rm n}) = \int_{E_{\rm c}}^{\infty} dE \, \mathcal{D}_{\rm n}(E) \left[1 + \exp\left(\frac{E - E_{\rm Fn}}{k_{\rm B} T_{\rm n}}\right) \right]^{-1},$$
 (1)

where $E_{\rm c}$ is the energy at the bottom of the conduction band, $k_{\rm B}$ is Boltzmann's constant, and $\mathcal{D}_{\rm n}$ is the DOS in the conduction band obtained from the full band structure. The DOS is obtained from the ν conduction bands in the usual way,

$$\mathcal{D}_{n}(E) = \sum_{\nu \text{ kin} \atop \text{BZ}} \delta[E - E_{\nu}(\mathbf{k})] = \sum_{\nu} \left(\frac{2}{(2\pi)^{3}} \int_{\text{BZ}} \frac{dS_{\text{E}}}{|\nabla_{\mathbf{k}} E_{\nu}(\mathbf{k})|} \right),$$

where δ is the Dirac delta function, and both the sum and the integral are over the constant energy surface $E_{\nu}(\mathbf{k}) = E$ for the ν th band in the Brillouin zone (BZ). The average electron energy $W_{\mathbf{n}}(E_{\mathbf{F}\mathbf{n}}, T_{\mathbf{n}})$ is given by

$$W_{\rm n}(E_{\rm Fn},~T_{\rm n})$$

$$= \frac{1}{n(E_{\rm Fn}, T_{\rm n})} \int_{E_{\rm c}}^{\infty} \frac{(E - E_{\rm c}) \mathcal{D}_{\rm n}(E)}{\left[1 + \exp\left(\frac{E - E_{\rm Fn}}{k_{\rm n} T_{\rm n}}\right)\right]} dE. \quad (2)$$

For $E_{\rm c}-E_{\rm Fn} \gg k_{\rm B}T_{\rm n}$, this reduces to $W_{\rm n}=3/2k_{\rm B}T_{\rm n}$. Equations (1) and (2) also define inverse relations $E_{\rm Fn}(n,\,W_{\rm n})$ and $T_{\rm n}(n,\,W_{\rm n})$; from Equation (1), the derivatives

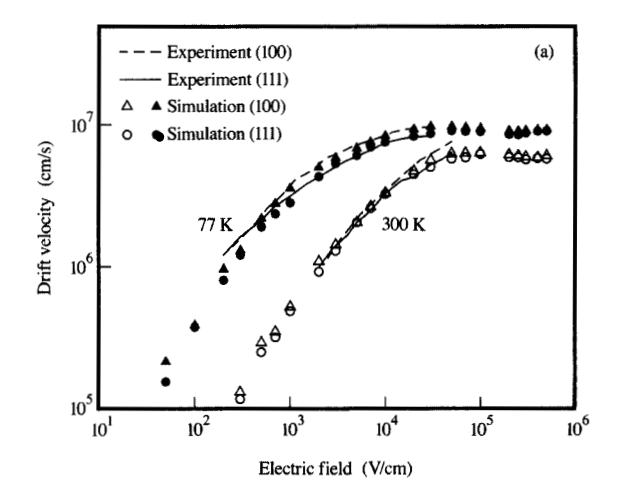
$$\left. \frac{\partial n}{\partial E_{\rm Fn}} \right|_{E_{\rm Fn}, T_{\rm n}, E_{\rm c} \, {\rm constant}} = - \left. \frac{\partial n}{\partial E_{\rm c}} \right|_{E_{\rm Fn}, T_{\rm n}, E_{\rm Fn} \, {\rm constant}}$$

may be obtained as well. Analogous relationships exist for holes in the valence band. These relationships are required in three contexts, to be discussed in turn: the Poisson equation, calculating screening lengths, and approximating degeneracy effects.

Solving the Poisson equation requires that the total charge density be evaluated. For a unipolar device model, the minority carrier charge density is determined by the potential and a constant quasi-Fermi level. In this case, the carrier Fermi energy and temperature (T_0 , the lattice temperature) are known and the density is sought. Furthermore, since the Poisson equation is solved by a damped Newton-Raphson iteration [69], the derivative of density with respect to E_c is needed. To evaluate ionization statistics for donors and acceptors, the assumption is made that donors are in equilibrium with the electrons and acceptors are in equilibrium with the holes. The quasi-Fermi energy obtained from the carrier density and average energy is used, together with the lattice temperature, to evaluate the fraction of dopants ionized. The derivatives $\partial N_{\rm D}^+/\partial E_{\rm c}$ and $\partial N_{\rm A}^-/\partial E_{\rm c}$ are likewise required by the Newton linearization and are readily obtained. Although not currently done, some time averaging of the carrier density used to set the quasi-Fermi levels for dopant ionization statistics would better account for the longer time constants involved in changing the charge state of the dopants.

Screening lengths are required to evaluate impurity and particle-particle scattering processes. The particle density and average energy are used to find the Fermi energy and particle temperature, from which the derivative of density with respect to Fermi energy is calculated. For particle-particle scattering, screening parameter β is evaluated as

$$\beta = e^{-\sqrt{\frac{1}{\epsilon} \left(\frac{\partial n}{\partial E_{\rm Fn}} + \frac{\partial p}{\partial E_{\rm Fp}}\right)}},\tag{3}$$



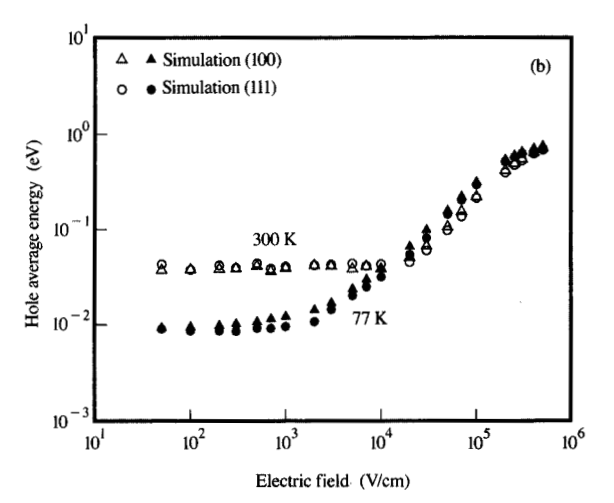
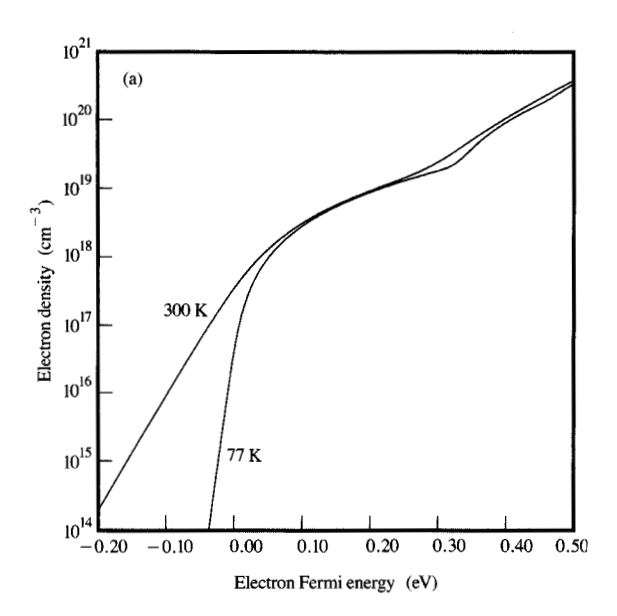
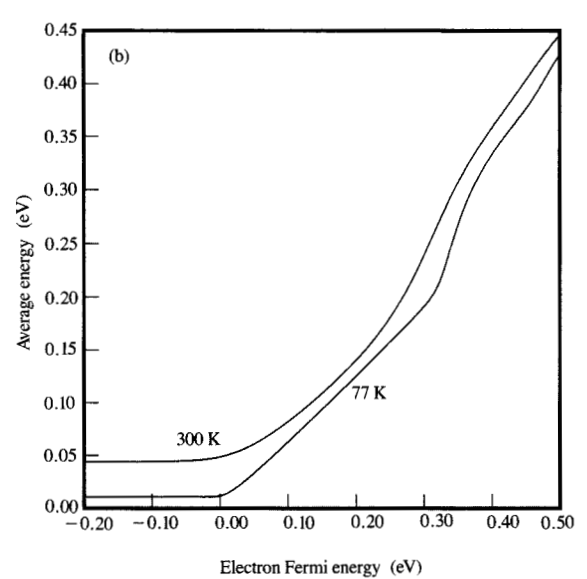


Figure 2

(a) Experimental behavior [65] and Monte Carlo simulation of hole drift velocity as a function of electric field along the (100) and (111) crystallographic directions in silicon, at 77 and 300 K. (b) Monte Carlo simulation of hole average energy in silicon, as a function of electric field along those crystallographic directions, at 77 and 300 K. From [63], reproduced with permission.

where ε is the permittivity and e is the magnitude of the electron charge. Equation (3) reduces to the Debye-Hückel and Thomas-Fermi expressions in the nondegenerate and degenerate limits, respectively. The values used in Equation (3) are backward-averaged in time in order to reduce statistical noise; the duration of this average is approximately 2-20 fs. For impurity scattering, Equation (3) is employed if $(n + p) > (N_D^+ + N_A^-)$; otherwise, the screening length is derived from the ionized impurity concentration





(a) Calculated electron density in GaAs as a function of electron Fermi energy, at temperatures of 300 and 77 K, as obtained from Equation (1). (b) Calculated electron average energy in GaAs as a function of electron Fermi energy, at the same temperatures, obtained from Equation (2).

$$\beta = e \sqrt{\frac{N_{\rm D}^+ + N_{\rm A}^-}{\epsilon k_{\rm B} T_0}}.$$
 (4)

Where β changes rapidly in space, our use of a screening sphere of constant radius is in error, as discussed previously [61]. This error could occur near the transition

from the channel to the source or drain, but is a small effect in the channel itself.

Degeneracy effects are approximated as previously described [61]. The approximate distribution function

$$f_{\text{app}}(E, \mathbf{r}, t) \simeq \frac{1}{1 + \exp\left[\frac{E - E_{\text{Fn}}(\mathbf{r}, t)}{k_{\text{B}} T_{\text{n}}(\mathbf{r}, t)}\right]},$$
 (5)

is evaluated with $E_{\rm Fn}$ and $T_{\rm n}$ obtained from the carrier density and average energy. The distribution function is then used to conditionally reject scattering events in order to statistically approximate the lack of final states under degenerate conditions.

Given their ubiquity, the actual evaluation of the integrals in Equations (1) and (2), their inverses, and the derivatives of density with respect to Fermi energy must be efficient. A table look-up approach is adopted; for electrons and holes, five tables each are constructed. For the case of electrons, the tables are as follows:

- $n(E_{\rm Fn}, T_{\rm n})$ and $W_{\rm n}(E_{\rm Fn}, T_{\rm n})$ are tabulated for $-0.2 \le E_{\rm Fn}$ ≤ +0.3 eV in 1-meV steps (up to +0.5 eV in 1.4-meV steps for GaAs) and $4 \le T_{\rm n} \le 25004$ K in 50-K steps.
- $E_{\rm Fn}(n,W_{\rm n})$ and $T_{\rm n}(n,W_{\rm n})$ are tabulated for $10^{11} \le n \le 10^{21}$ cm⁻³ in 500 logarithmic steps and $0.005 \le W_{\rm n} \le 2.155$ eV in 4.3-meV steps.
- $\partial n/\partial E_{\rm Fn}$ ($E_{\rm Fn}$, $T_{\rm n}$) is tabulated for $-0.2 \le E_{\rm Fn} \le +0.3$ eV in 1-meV steps (up to +0.5 eV in 1.4-meV steps for GaAs) and 4 ≤ $T_{\rm n} \le 25004$ K in 50-K steps.

In addition, extrapolation outside the table is used where well-defined limits exist (e.g., the Boltzmann regime); otherwise, program execution is stopped. Examples of results obtained following this procedure are shown in Figure 3. For the case of the conduction band in GaAs, the electron density (a) and average energy (b) are plotted against the Fermi energy at 300 and 77 K. The electron density shows Boltzmann-like behavior for sufficiently negative Fermi energies, with the expected exponential fall-off evident from the curve. As the electron Fermi energy moves into the conduction band $(E_{\rm Fn} > 0)$, the density of states, together with the Fermi function, determines the electron density. The Γ valley is populated for $E_{\rm Fn} \lesssim 0.25$ eV, with the structure in the density around 0.3 and 0.45 eV representing the L valleys and X valleys, respectively, contributing to the total density of states. In Figure 3(b), the average electron energy is shown for the same conditions. For $E_{\rm Fn} \lesssim 0$, the Boltzmann limit $W_n = 3/2k_BT_n$ is approached. For increasing degeneracy, the average energy climbs, since the exclusion principle forces progressively higher energy states to be occupied. Again, this curve has structure evident around 0.3 and 0.45 eV, attributable to the L valleys and X valleys, respectively.

• Statistical enhancement of rare events

Results obtained via Monte Carlo device simulation are only as good as the statistical variance of the estimators of particle behavior. Unless special provisions are made. the particles will only probe spatial regions of the device with the highest carrier densities, and energy intervals favored by the local energy distribution function. Finite central processing unit (CPU) budgets and particle counts preclude a "brute force" solution to this problem. This difficulty can be circumvented by dividing the ensemble into "common" and "rare" populations, and assigning "rare" particles a reduced statistical significance [70]. Such a procedure has been described recently in the context of Monte Carlo MOSFET simulation [71]. A similar scheme has been implemented in DAMOCLES, but with an important improvement: The number of particles in "rare" configurations is automatically adjusted to maintain a target particle population. By keeping a known number of particles in a rare state, statistical variance within that state can be controlled.

The DAMOCLES program accepts as input the boundaries in space and kinetic energy where statistical enhancements are to occur. Many such regions may be defined. In each region (called a "stat-box"), a target number of particles is also specified, as a fraction of the total number of particles nominally desired in the model. As the simulation proceeds, stat-boxes are processed as follows. Particles crossing stat-box boundaries are replicated, or conditionally removed, according to the relative statistical weights of the two regions. A stat-box with no particles initially becomes active when first entered by particles, inheriting the average statistical significance of the entering particles. Then, statistical weights within individual stat-boxes are adjusted so that the particle count in any box containing particles is within 20% of the target value of the box. This target value is also adjusted, to ensure that unpopulated statboxes do not artificially lower the total number of particles nominally present in the device. The stat-boxes for electrons and holes are totally independent, allowing vastly different spatial and energy configurations to be accurately resolved for each carrier type. Besides the complexity introduced in "bookkeeping" by this method, care must be taken to handle the short-range particleparticle interaction correctly. In our method, described previously [61], the total energy of the ensemble is statistically conserved in the presence of interactions between particles of differing statistical significance.

3. Submicron silicon MOSFET results

In this section we present simulation results for both n- and p-channel silicon MOSFETs at an operating temperature T of 77 and 300 K. The n-MOSFETs discussed here are identical to devices discussed in the

context of off-equilibrium transport [61-63], and are based on experimental devices of Sai-Halasz et al. [72– 74]. The p-MOSFETs simulated here are simply derived from the n-MOSFET cross section by inverting the polarity of the doping, the gate work function, and the applied bias. Such p-MOSFETs are probably not technically feasible: The degenerately doped antimony n⁺ sources and drains in these n-MOSFETs have extremely sharp doping gradients, but there is no way to duplicate this sharp source/drain profile with an acceptor dopant for the p-MOSFETs. Such p-MOSFETs remain of interest, however, since comparisons with corresponding n-MOSFETs are not clouded by differences in geometry or doping. Rather, the comparison quantifies the intrinsic differences in electron and hole transport. Preliminary p-MOSFET simulation results have been published [63], but the emphasis in this paper is on comparing MOSFETs with different channel lengths and applied biases for 300- and 77-K operating temperatures. Unless otherwise specified, particle-particle scattering is not in effect for these MOSFET simulations. The average energies, velocities, etc., so obtained do differ somewhat from their counterparts obtained with particle-particle scattering (see Section VI.-B in [61]), but the qualitative behavior is similar, and this decision does not seriously detract from the subsequent discussion.

• Comparison of p- and n-MOSFET results

The n- and p-channel devices are simulated for T=300 and 77 K, and equal $|V_G|$ and $|V_D|$. The source/drain doping is assumed to form very nearly a step junction, having a lateral Gaussian straggle of 5 nm and a peak concentration of $\sim 1.5 \times 10^{20}$ cm⁻³. A Gaussian channel threshold-adjust implantation is included, with a peak density of 7×10^{17} cm⁻³ occurring 70 nm below the Si-SiO₂ interface, with a straggle of 30 nm. The background substrate doping is chosen to be 6.5×10^{15} cm⁻³. The oxide is assumed to be 4.5 nm thick. Both devices are surface channel devices, as the n-MOSFET contains an n⁺ poly gate, and the p-MOSFET contains a p⁺ poly gate. For the n-MOSFET, the source/drain is n-type, and the substrate and channel implant are p-type; for the p-MOSFET, the complement is true.

Figure 4 shows the Monte Carlo particle total energy distribution at an instant in time along the interface of n- and p-MOSFETs, assuming that their metallurgical channel lengths $L_{\rm CH}$ are 233 nm, $|V_{\rm G}|=|V_{\rm D}|=2.5$ V, their sources and substrates are grounded, and T=300 K. The particles are colored in 50-meV increments according to kinetic energy, ranging from 0 eV (blue) to 1.0 eV (red). The conduction and valence band potentials are shown as cyan curves in (a) and (b), respectively. The displacement of a particle away from the potential energy curve gives a second indication of kinetic energy. Note

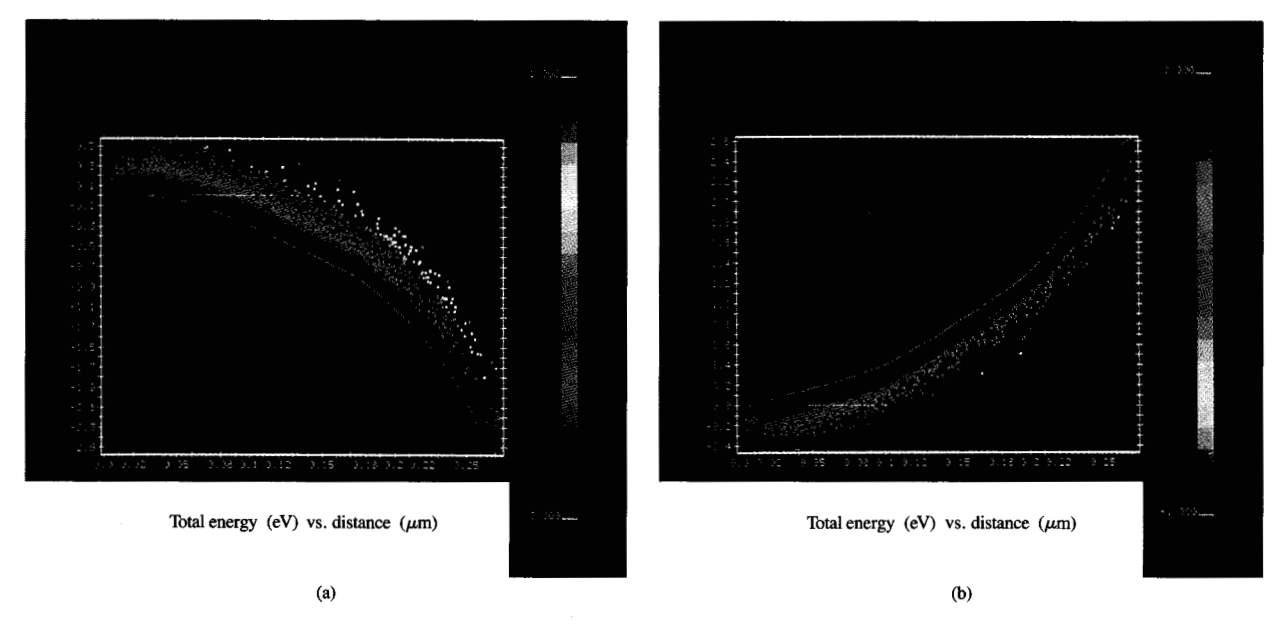


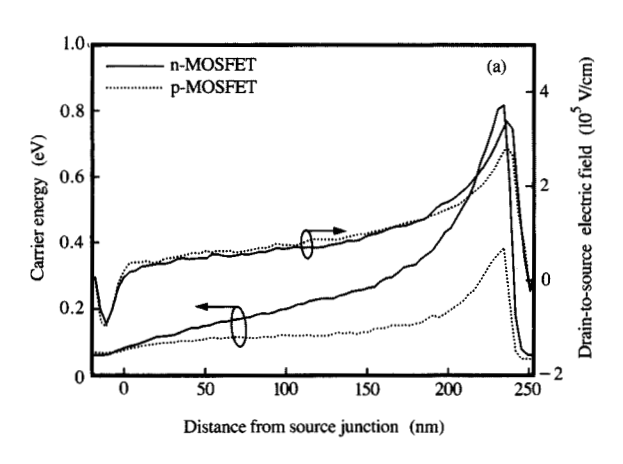
Figure 4

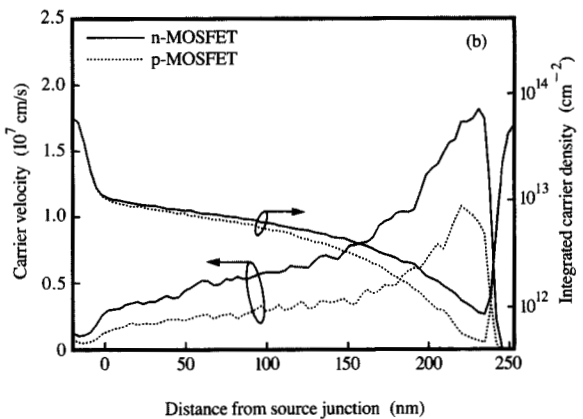
Calculated distribution in total energy of the Monte Carlo particles along the Si-SiO₂ interface for (a) an n-MOSFET and (b) a p-MOSFET for the following conditions: $L_{\rm CH}=233$ nm, $|V_{\rm G}|=|V_{\rm D}|=2.5$ V, source and substrate grounded, and T=300 K. The metallurgical channel is assumed to extend from 0.020 to 0.253 μ m. Electrons in (a) and holes in (b) are colored according to their kinetic energy.

that the electron energy increases upward, while the hole energy increases downward. Only particles within 10 nm of the interface are shown. In the n-MOSFET (a), the electrons remain in a tight energy distribution for approximately the first half of their journey from source to drain, and show nonequilibrium behavior only near the drain end of the channel. In the p-MOSFET (b), holes show markedly less broadening in the particle distribution as carriers move from source to drain. This result is expected, since the scattering rate is higher for holes than for electrons. This implies shorter mean free paths for holes, with the commensurate increased difficulty of achieving quasi-ballistic behavior. Figure 5 compares quantitatively carrier energy, velocity, and density and the electric field in these devices. In Figure 5(a), the carrier kinetic energy and the drain-to-source electric field are shown. Moving in virtually the same field pattern, electrons gain roughly twice as much kinetic energy as holes, due to their different transport behavior. In Figure 5(b), the carrier velocity and carrier density (integrated perpendicular to the interface) are shown. The velocity attained by electrons exceeds their saturated velocity of 0.96×10^7 cm/s near the drain, while holes only reach a peak velocity of 1.1×10^7 cm/s. However, this velocity does exceed the saturated velocity for holes $(0.62 \times 10^7 \text{ cm/s})$ in the pinch-off region. The integrated carrier density in the channel is qualitatively similar,

becoming somewhat different near the drain. Near the source, the inversion charge is slightly less for the p-MOSFET due to an effective difference of ~0.06 V in applied gate voltage, caused by the difference in built-in potential at the source/drain contacts for n⁺ versus p⁺ material, even when doped to the same magnitude. This results in a slight bias asymmetry, with the p-MOSFET being slightly more pinched off than the n-MOSFET. Near the drain, the p-MOSFET density is depressed relative to the n-MOSFET because of this slight internal bias asymmetry and because of the requirement of current continuity in the channel: The ratio of the carrier velocity in the pinch-off region to the carrier velocity in the channel is higher for the p-MOSFET than for the n-MOSFET.

Figure 6 shows the calculated Monte Carlo particle total energy distribution at an instant in time along the interface for an n- and a p-MOSFET with $L_{\rm CH}=53$ nm. The applied biases are assumed to be $|V_{\rm G}|=|V_{\rm D}|=0.8$ V, with the source and substrate grounded; the operating temperature T is assumed to be 77 K. For both the n-MOSFET (a) and the p-MOSFET (b), a behavior qualitatively different from that shown in Figure 4 is seen. The width of the energy distribution increases steadily in moving from source to drain. Local equilibrium, i.e., an interval where a single kinetic energy distribution can be slid along the potential energy curve





(a) Carrier energy and drain-to-source electric field as a function of distance along the interface, calculated for the n- and the p-MOSFETs of Figure 4. Both quantities have been averaged over a depth of 10 nm below the interface. (b) Calculated carrier velocity and integrated carrier density as a function of distance along the interface, for the same MOSFETs. The velocity is in the source-to-drain direction, and has been averaged over a depth of 10 nm below the interface.

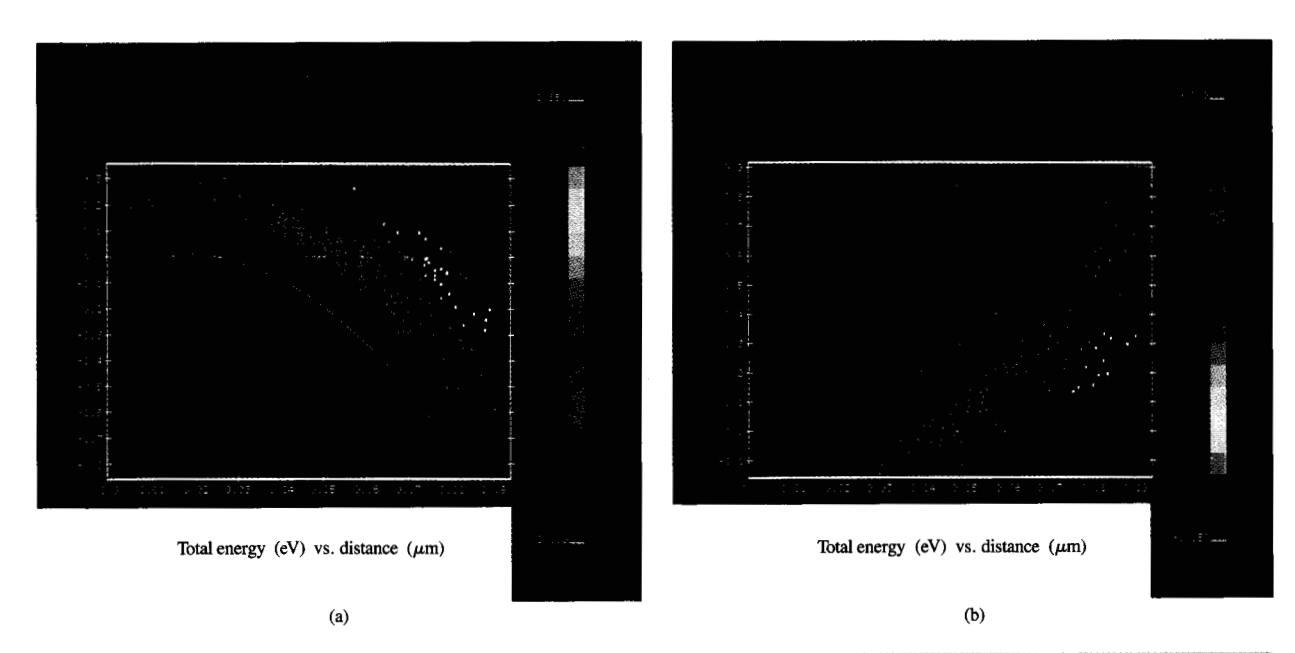
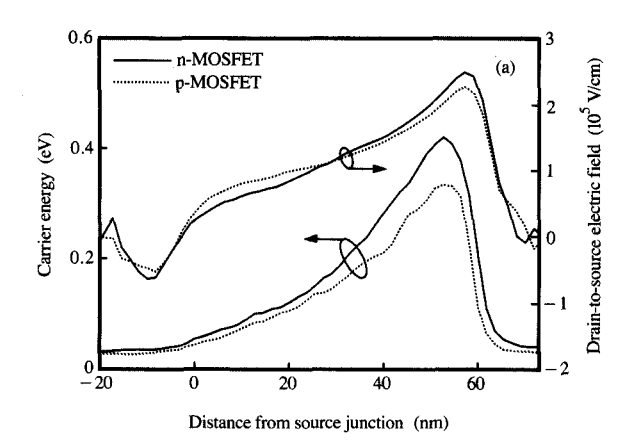


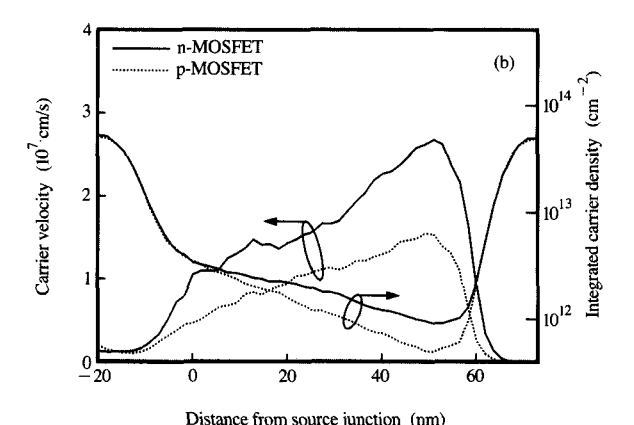
Figure 6

Calculated distribution in total energy of the Monte Carlo particles along the Si-SiO₂ interface for (a) an n-MOSFET and (b) a p-MOSFET. For each it is assumed that $L_{\rm CH}=53$ nm, $\mid V_{\rm G}\mid=\mid V_{\rm D}\mid=0.8$ V, source and substrate are grounded, and T=77 K. The metallurgical channel is assumed to extend from 0.020 to 0.73 μ m. Electrons in (a) and holes in (b) are colored according to their kinetic energy.

and remain a good representation (this tacitly assumes a constant channel field), is present nowhere in the channel. The shorter distance scale, together with the

lower temperature, conspires to make mean free paths longer relative to the channel length. This increases the importance of velocity overshoot in this case. Figure 7





(a) Carrier energy and drain-to-source electric field as a function of distance along the interface, calculated for the n- and the p- MOSFET of Figure 6. Both quantities have been averaged over a depth of 10 nm below the interface. (b) Calculated carrier velocity and integrated carrier density as a function of distance along the interface, for the same MOSFETs. The velocity is in the source-to-drain direction, and has been averaged over a depth of 10 nm below the interface.

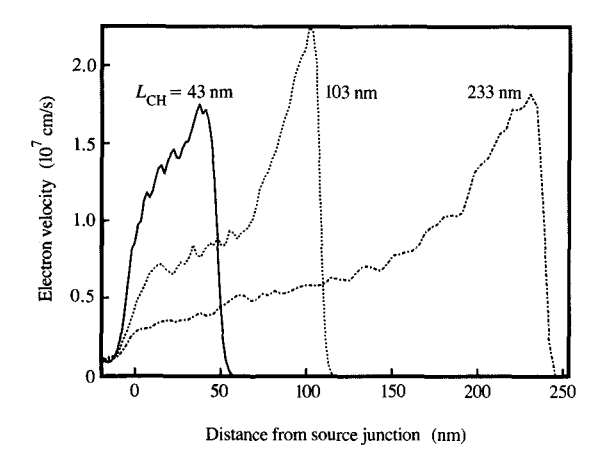
shows the calculated carrier energy, velocity, and density and the electric field for the devices of Figure 6. Again, electrons in the n-MOSFET gain more kinetic energy than holes in the p-MOSFET, although the electric field is similar in magnitude in both devices, as seen in Figure 7(a). Note that the average energy cannot significantly exceed the drain voltage, 0.8 V. The average energy approaches the drain voltage as pure ballistic transport across the channel becomes dominant. Figure 7(b) shows the carrier velocity, indicating the presence of velocity overshoot. At 77 K, the saturated velocity $v_{\rm sat}$ for electrons is 1.2×10^7 and for holes is 0.98×10^7 cm/s. In

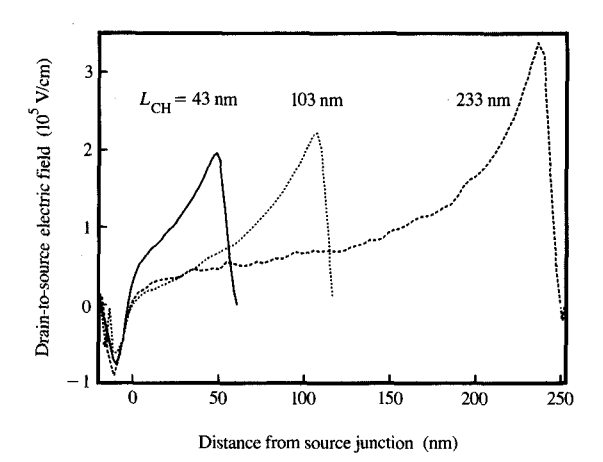
the n-MOSFET, the electron velocity exceeds $v_{\rm sat}$ over nearly the entire channel; for the p-MOSFET, the hole velocity exceeds $v_{\rm sat}$ over approximately half the channel. The hole density is lower than the electron density near the drain. Again, current continuity forces this, as the ratio of the peak carrier velocity to the carrier velocity at the source junction is larger for the p-MOSFET than for the n-MOSFET.

The transconductance for these n-MOSFETs has been discussed previously [61, 62]. We add here only that the calculated current and transconductance for the complementary p-MOSFETs are roughly half those of their n-MOSFET counterparts. This preliminary result seems true both at 300 and 77 K, at the 233-nm channel length level. For sub-100-nm devices, the p-MOSFET transconductance makes modest gains relative to the n-MOSFET, approaching 75% of the n-MOSFET result.

• Nonequilibrium transport: Channel length dependence The importance of nonequilibrium transport increases as the device channel length decreases. It is instructive, however, to compare on an absolute scale the internal device behavior as a function of channel length. Consider a trio of n-MOSFETs, differing only in metallurgical channel length ($L_{CH} = 43$, 103, and 233 nm). The biases applied to the three are scaled roughly with the channel length, i.e., along the lines of constant field scaling. For the 43-nm device, $V_G = 0.7$ and $V_D = 0.6$ V. For the 103-nm device, $V_G = 1.0$ and $V_D = 1.0$ V, and for the 233-nm device, $V_G = 2.5$ and $V_D = 2.5$ V. The source and substrate are assumed to be grounded in all cases. The average drain field across the 43-, 103-, and 233-nm channels is therefore 1.40, 0.97, and 1.07×10^5 V/cm, respectively. The lattice temperature is assumed to be 300 K. We now consider the electron velocity and kinetic energy in the MOS channel.

Figure 8 shows the calculated electron velocity along the interface, averaged over a 10-nm depth below the interface. Since $v_{\text{sat}} = 0.96 \times 10^7 \text{ cm/s}$, significant portions of the channel length exceed v_{sat} for each device. The maximum velocity is always achieved at the drain junction. The behavior of the velocity qualitatively changes from longest to shortest channel length: For the 233-nm device, the velocity grows slowly in the first two thirds of the channel, and then increases rapidly in the last third. This is consistent with "long-channel" device behavior, with linear and pinch-off channel regions well delimited. The behavior of the 103-nm device is similar, with the division occurring midway along the channel. For the shortest device, the velocity rises rapidly starting at the source. The velocities obtained by dividing the metallurgical channel by the transit time across the channel for the three devices are 1.34, 0.90, and 0.60×10^7 cm/s, clearly reflecting the role of velocity





5.6177

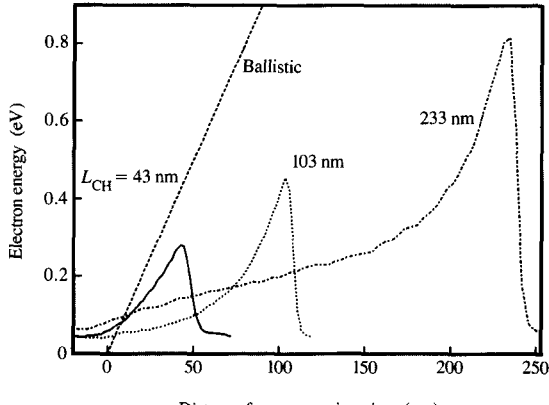
Calculated electron velocity for three Si n-MOSFETs plotted against the distance along the interface. For the $L_{\rm CH}=43$ -nm device, it is assumed that $V_{\rm G}=0.7$ V and $V_{\rm D}=0.6$ V; for the 103-nm device, it is assumed that $V_{\rm G}=1.0$ V and $V_{\rm D}=1.0$ V; and for the 233-nm device, that $V_{\rm G}=2.5$ V and $V_{\rm D}=2.5$ V. Sources and substrates are assumed to be grounded; T is assumed to be 300 K. The velocity is in the source-to-drain direction, averaged over a depth of 10 nm below the interface.

Figure 9

Calculated drain-to-source electric field as a function of distance along the interface, for the three devices of Figure 8, averaged over a depth of 10 nm below the interface.

overshoot for the smallest device. Note, however, that the 103-nm device has the highest peak velocity of the three. This occurs because the peak velocity is determined both by the initial velocity entering a region of high field and by the distance over which the field acts. Figure 9 shows the drain-to-source electric field for the three devices. Again, the 233-nm device shows "long-channel" behavior, namely, a distinct channel field ($\sim 0.5 \times 10^{5}$ V/cm) and pinch-off region. The behavior of the 103-nm device is similar, but with a much shorter linear region. No such distinction is present in the shortest device, for the field is becoming more uniformly spread over the channel. The high-field regions of the three curves have qualitatively the same shape and distance scale, extending back from the peak $\sim 50-75$ nm. This fixed distance consumes progressively more of the channel as the channel length shrinks.

Figure 10 shows the electron kinetic energy for the three devices, averaged over a 10-nm depth below the interface. The maximum energy occurs in the longest device. The peak energy is determined by many factors, but the limiting cases are clear: For pure ballistic transport, peak kinetic energy is set by the drain bias, while in equilibrium with an electric field of 10⁵ V/cm, electrons are heated to an average kinetic energy of ~0.65 eV. The occurrence of low energies in the smallest

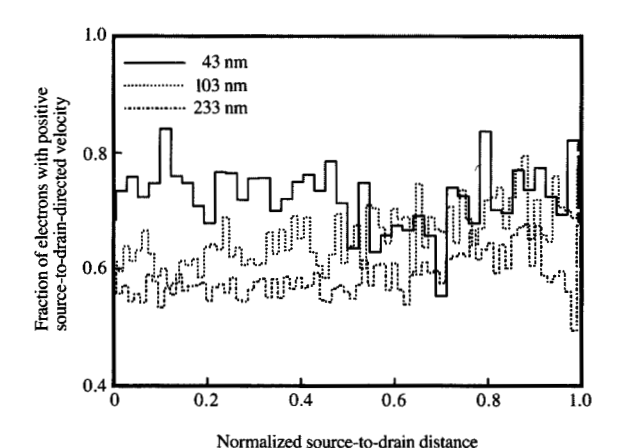


Distance from source junction (nm)

Floring

Calculated electron energy as a function of distance along the interface, for the three devices of Figure 8, averaged over a depth of 10 nm below the interface. The energy that ballistic electrons leaving the source would obtain in a fixed field of 10⁵ V/cm is shown for comparison.

devices where velocity overshoot is most significant is no accident: Carriers colder than dictated on the basis of equilibrium with the local field experience relatively less scattering, and are free to fly in the field and attain high

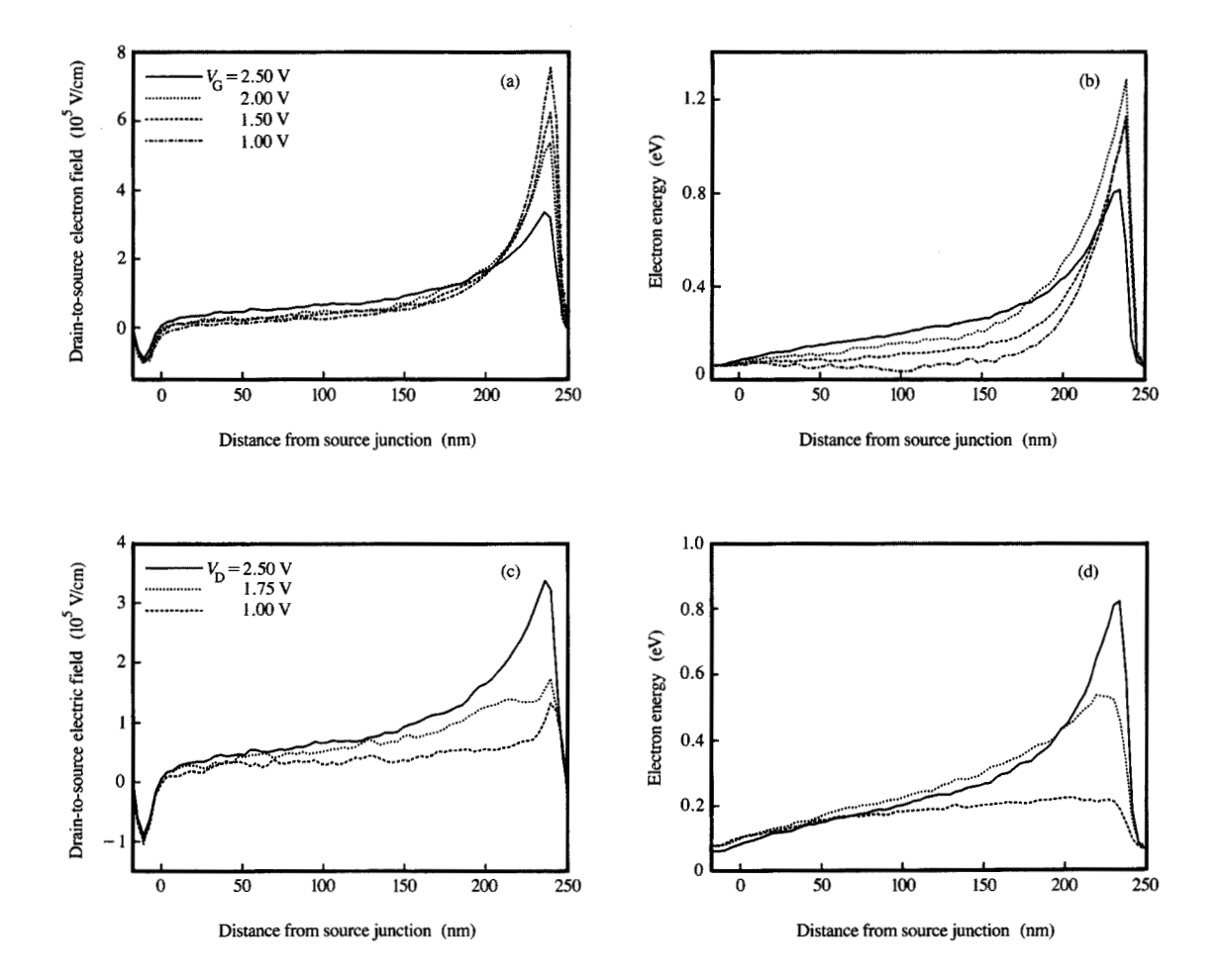


Fraction of electrons with velocity directed from source to drain versus the normalized source-to-drain distance, calculated for the three devices of Figure 8.

velocities. This is clearly the case here. However, this does not explain the behavior near the source in Figure 10, where the energy in the longest device is larger than in the shorter devices. This higher energy accompanies the "long-channel" behavior referred to previously. A local equilibrium is established near the source in the 233-nm device, with an electron energy consistent with the local field there. Alternatively, this can be regarded as a state in which the fraction of electrons with positive (source-to-drain) velocity relative to the whole is that corresponding to local equilibrium with the field. Electrons accelerated toward the drain by the drain field have a sufficient distance in which to be backscattered, raising the average energy near the source. In the shorter devices, this flux of backscattered electrons is progressively reduced because the drain collects electrons before they can scatter backward in the channel. This point is clarified in Figure 11, where the fraction of electrons with positive-going velocity is given for the three devices. For pure ballistic transport with no possibility of backscattering, this fraction becomes 1.0; for zero net current flow, the value would be 0.5. Note that near the drain the curves come closer together, indicative of the higher scattering rates of the hot carriers there driving the system toward local equilibrium with the high field over a shorter distance scale. We note, finally, that the results of Figures 8-11 are qualitatively unchanged at 77 K, with peak velocities and energies increasing ~1.6-1.7 times over the values shown for 300 K.

 Nonequilibrium transport: Bias dependence The results of the previous subsection are now revisited from a different perspective: Assuming that the n-MOSFET geometry and lattice temperature are fixed, the electric field and electron energy are discussed as a function of the device bias. In Figure 12 we consider a 233-nm n-MOSFET at 300 K. The substrate and source are assumed to be grounded. For Figure 12(a, b), $V_{\rm p} = 2.5 \text{ V}$ is fixed, while the gate voltage varies. For Figure 12(c, d), $V_G = 2.5 \text{ V}$ is fixed, while the drain voltage varies. The calculated drain-to-source electric field along the interface is shown in Figure 12(a, c); the electron energy is shown in Figure 12(b, d). In Figure 12(a), the electric field has a "long-channel" appearance, with well-delineated linear and pinch-off regions. As the gate bias is decreased, the channel field decreases slightly and the field near the drain grows larger, consistent with a stronger pinch-off of the channel. Figure 12(b) shows the electron energy in this case. As the gate bias decreases, the channel energy decreases. The energy rises at the drain end of the channel, but the highest energy peak is not attained at the lowest gate bias. Although the electrons are heated by the high field near the drain in every case, the lower energy of electrons entering the pinch-off region manages to lower the peak energy attained for $V_G \le 1.50 \text{ V}$. The peak average energy falls well short of the drain voltage, as expected. The same quantities are shown in Figure 12(c, d), but for a constant $V_{\rm c} = 2.5$ V. As the drain voltage decreases, the device operates in the triode region. The entire channel becomes more like a linear resistor, and the field becomes more uniform over the channel, as seen in Figure 12(c). Figure 12(d) shows that the energy becomes more uniform as well, and decreases in response to the lower field values.

The previous results for a 233-nm n-MOSFET at 300 K can now be compared to results obtained for a 43-nm device operating at 77 K. Figure 13 depicts the same information for this shorter device. In Figure 13(a), the electric field is smoother, even for the lowest gate voltage. The sharp increase in the field, and the obvious division of the channel into linear and pinch-off regions seen in Figure 12(a), is absent. The corresponding energy is shown in Figure 13(b), where the energy is remarkably impervious to the change in gate voltage. The energy gain is primarily determined by the drain bias (1.0 V), a sign of the dominance of nonequilibrium transport. Only the energy rise in the channel differs, being fastest when the field near the source is highest. Figure 13(c) shows the electric field when $V_G = 1.0 \text{ V}$ is held constant. Reducing the drain bias moves the device into triode region operation, and the field simultaneously becomes lower and more evenly spread over the channel. This is similar to the result in Figure 12(c) for the 233-nm device. Finally, Figure 13(d) gives the corresponding electron



Calculated electric field and electron energy distributions along the interface, for a 233-nm-channel-length n-MOSFET at 300 K under various bias conditions. The substrate and source are assumed to be grounded. (a) Drain-to-source electric field as a function of distance, for fixed $V_{\rm D}=2.50$ V. (b) Electron energy corresponding to the bias conditions of (a). (c) Drain-to-source electric field versus distance, for fixed $V_{\rm G}=2.50$ V. (d) Electron energy corresponding to the bias conditions of (c).

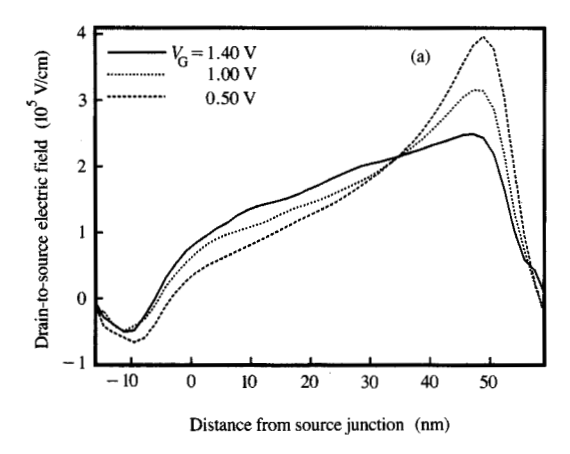
energy, which tracks the behavior of the field by becoming lower and more uniform in the channel. This parallels the behavior shown in Figure 12(d).

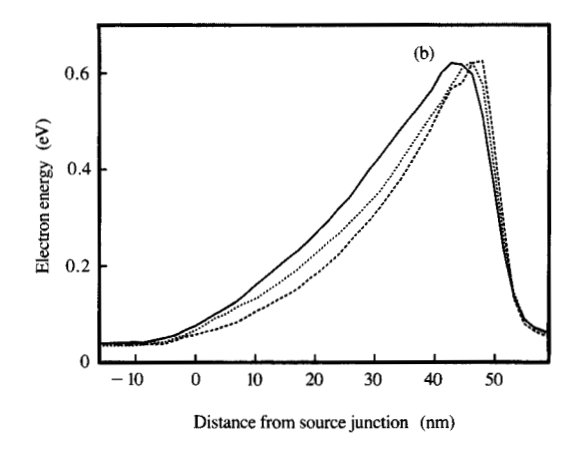
Comparing the 233-nm, 300-K behavior shown in Figure 12 to the 43-nm, 77-K device results of Figure 13 shows fundamental differences for high drain field conditions. For the larger device, "long-channel" behavior is seen, with distinct linear and pinch-off regions in the channel. The energy gained is primarily at the drain end of the channel. The 43-nm device has a smoother field pattern, with no distinction possible in the channel between linear and pinch-off intervals. The energy gained is limited by the applied drain bias due to

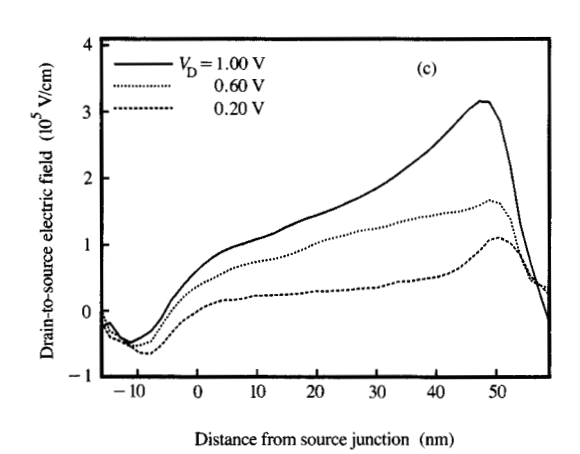
the strong off-equilibrium transport in this short channel. For low drain bias operation, however, both devices operate analogously, although the field pattern remains more smeared out over the channel of the 43-nm device.

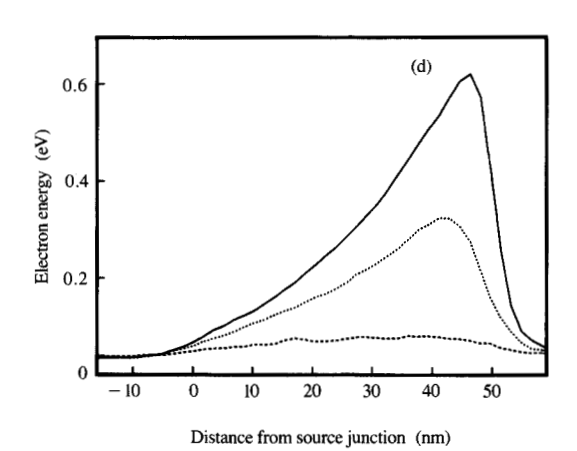
■ Interface scattering

In the DAMOCLES program, a combination of specular and diffuse elastic scattering has been employed at the Si-SiO₂ interface. A more rigorous approach would be to utilize explicit surface scattering mechanisms, such as Coulomb and surface roughness scattering. However, only by introducing quantization in the channel will the distance between the carriers and the interface be









Floure 13

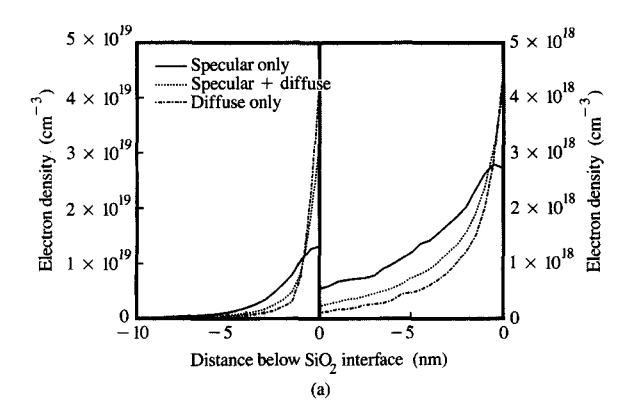
Calculated electric field and electron energy distributions along the interface for a 43-nm-channel-length n-MOSFET at 77 K under various bias conditions. The source is assumed to be grounded and the substrate forward-biased by 0.6 V. (a) Drain-to-source electric field as a function of distance, for fixed $V_{\rm D} = 1.00$ V. (b) Electron energy corresponding to the bias conditions of (a). (c) Drain-to-source electric field versus distance, for fixed $V_{\rm G} = 1.00$ V. (d) Electron energy corresponding to the bias conditions of (c).

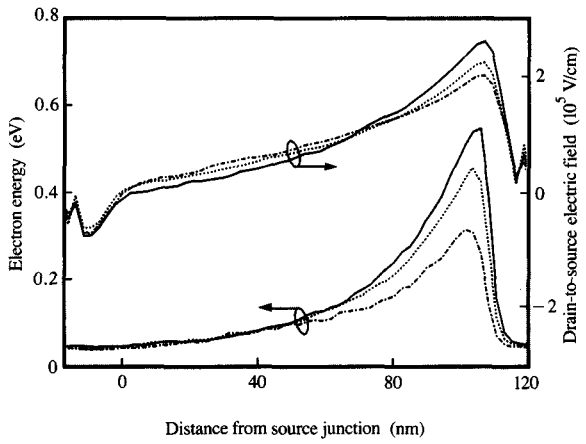
correctly represented. Lacking quantization in the channel in the present program, the simpler representation of interface scattering is considered acceptable.

Specifically, in the previous subsection, an equal probability for specular and diffuse scattering was used. However, the results are sensitive to the exact ratio of specular and diffuse interface scattering. Specular scattering is defined as an elastic deflection by the interface where momentum perpendicular to the interface is reversed; i.e., the reflected angle equals the incident angle. The diffuse scattering assumed here is

slightly nonstandard: The particle is assumed to be scattered into a k-state chosen from among all final states which conserve energy and yield a velocity directed away from the SiO_2 , with a probability proportional to the DOS at k. Let s be the probability for specular scattering $(0 \le s \le 1)$, with (1 - s) the probability for diffuse scattering. As s increases from 0 to 1, the ability of the interface to change the direction of electron motion in the source-to-drain direction decreases. By reducing the probability of backscattering the source-to-drain motion of an electron, the inversion layer mobility increases as s increases. This has the net effect of reducing the

resistance of the linear channel region. This effect is portraved in two different ways in Figure 14, where results for an n-MOSFET with a 103-nm channel length operating at 300 K are shown. Both drain bias and gate bias are assumed to be 1.0 V. The case of an equal probability of specular and diffuse scattering (s = 0.5) is compared to the case where only specular scattering, or only diffuse scattering, is included. In (a), a plot of electron density perpendicular to the interface is shown, at 20% (left) and 80% (right) of the way down the channel from the metallurgical source junction. The electron density spreads out more below the interface as the amount of specular scattering is increased. This is explained as follows. First, consider the source end of the channel. Here in the linear portion of the channel, the amount of inversion charge induced by the gate field is fixed by the oxide capacitance and the gate drive (gate voltage above the threshold voltage). This is a consequence of Gauss' law. Thus, the area under each of the curves in (a) at the source end must be equal. Also, the channel current increases monotonically with s, since the channel mobility increases and the bias is fixed. The source/drain currents vary by more than 2.5 times as s changes: for s = 0, 0.5, and 1.0, the current is 1.56, 2.81,and 4.18 A/cm, respectively. Although the field decreases in the channel as s increases, the power input to the electrons in the channel still increases with s, making the electrons hotter and causing them to spread out further below the interface (~40 meV hotter for specular compared to diffuse near the source). As a minor secondary effect, our model of diffuse scattering is somewhat more likely to redirect electrons parallel to the interface (in the two-dimensional modeling plane). For example, for 40-meV electrons scattered diffusely by the interface, the electrons are ~30% more likely to be deflected along the interface (either forward or backward) compared to a model for diffuse scattering directing particles outward uniformly in a semicircle. Our model is ~10% less likely to place particles in trajectories directed near 45° relative to the interface. Exit trajectories perpendicular to the interface are equally likely in either model of diffuse interface scattering. These differences stem from differences in the DOS as a function of the exit angle. The effect here, then, is for our diffuse scattering to increase slightly the time an electron spends near the interface; this further increases the electron concentration near the interface as diffuse scattering dominates. The spread below the interface is summarized by the first moment of the electron density, which is located 0.85, 1.15, and 1.85 nm below the interface, for s = 0, 0.5, and 1.0, respectively, at the source end of the channel. Near the drain end of the channel, the behavior persists, due to the differing electron energies in the three cases.



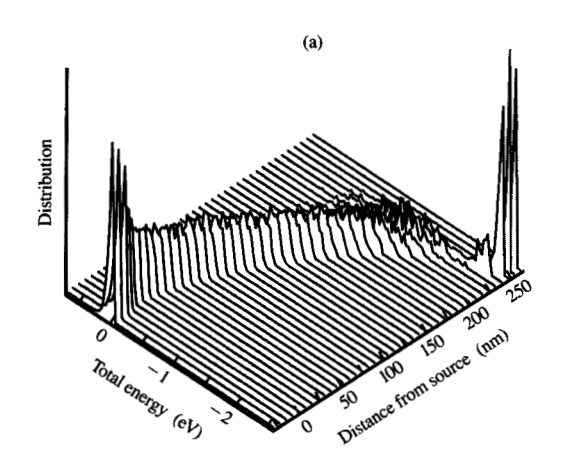


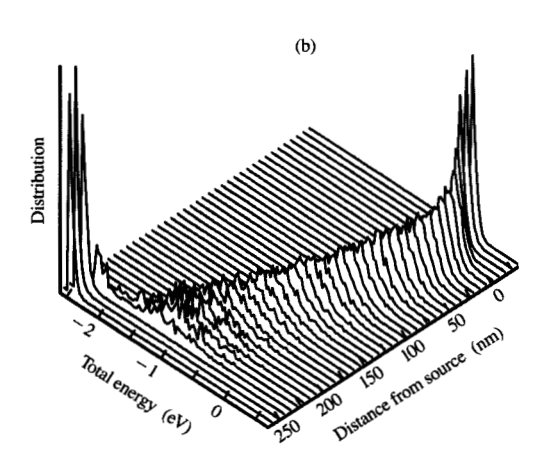
(b)

FIGURE 16

(a) Calculated electron density versus position below the ${\rm SiO}_2$ interface, for 20% (left) and 80% (right) along the channel from the metallurgical source junction, for three different interface scattering models. An n-MOSFET with $L_{\rm CH}=103$ nm and $V_{\rm G}=V_{\rm D}=1.0$ V is considered at 300 K. (b) Calculated electron energy and drain-to-source electric field plotted against distance from the source junction, for the same conditions in (a), averaged over a depth of 10 nm below the interface.

In Figure 14(b), the electron energy and drain-to-source electric field are plotted as a function of the distance from the source junction. The electron energy is averaged over a 10-nm depth below the interface, and hence does not show the energy difference in the inversion channel attributed to the differing power inputs discussed directly above, since the inversion layer is much thinner than 10 nm. Near the drain, however, the differing electron energies are clearly seen. As *s* increases, the peak energy and field both increase. The peak field increases as *s* increases because of a lower channel field, brought about by the lower resistance in the channel.





Electron total energy distributions calculated for a 233-nm-channel-length n-MOSFET at 300 K. Biases are assumed to be the same as for Figure 4(a). The 40 distributions stacked adjacent to one another are all normalized to have the same area. The same data are shown in (a) and (b), derived from opposite viewpoints.

This higher pinch-off field also accounts for the higher peak energy. Our selection of s=0.5 in other subsections was made arbitrarily, wishing to favor neither individual interface scattering process. Although comparisons to experimental data have been favorable [61, 62], a more rigorous model of surface scattering is certainly desirable.

• Distributions

The real power of a Monte Carlo modeling approach is the ability to evolve the distribution function which solves the Boltzmann transport equation (BTE). Deterministic approaches to solving the BTE in device modeling either assume a form for the distribution function a priori, or solve a truncated system of equations derived from taking velocity moments of the BTE. A Monte Carlo method avoids this approximation altogether. A distinct disadvantage, however, is that rare events must be amplified, and although such procedures are available [70], some knowledge of where to look for rare events is usually required. Fortunately, regions where hot-carrier distributions are sought are generally known beforehand. Quantifying these hot-carrier populations and their effect on device degradation is an extremely important requirement for a program like DAMOCLES.

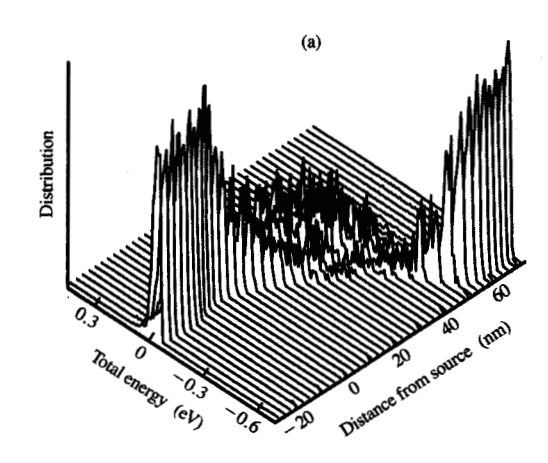
Figure 15 shows the calculated distribution in total energy of electrons in a 233-nm-channel-length n-MOSFET at 300 K. The device geometry is sliced into 40 equal sections perpendicular to the interface, and the steady-state kinetic energy distribution is calculated in each section. These 40 energy distributions are all normalized to have the same area. This normalization to equal areas enlarges the high-energy tails in low-density regions (the channel) relative to those in the source/drain, but has still proven superior to other normalizations examined. Finally, the distributions are stacked adjacent to one another and offset by the local potential energy in the channel. In Figures 15(a) and 15(b) the same data are plotted from two different viewpoints. In Figure 15(a), the trace of the potential energy in the channel is clearly shown by the points of lowest total energy where the distribution becomes nonzero. Figure 15(b) shows more clearly the manner in which the hot tail of the distribution changes over the channel length. This figure is based on the same device shown in Figure 4(a), and the local equilibrium behavior in the first half of the channel is now easier to see.

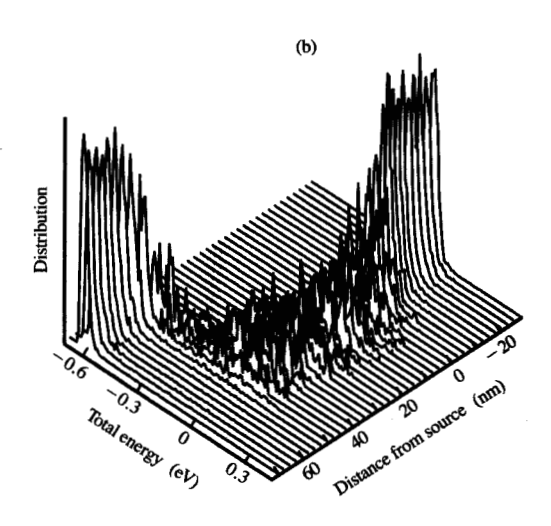
The strong off-equilibrium transport present in the 53-nm n-MOSFET operating at 77 K is shown in the total energy distribution of **Figure 16**. Again, two views of the same data are shown. The tendency toward ballistic transport across the channel is indicated by the distribution remaining at nearly a constant total energy over the channel length. The device and bias were previously described in conjunction with Figure 6(a).

Electron wave-vector distributions supplement energy distributions as an additional way to underscore the off-equilibrium transport present in these small MOSFETs. Consider an n-MOSFET with a channel length of 233 nm, operating at 77 K with $V_{\rm G} = V_{\rm D} = 2.5$ V. Electrons within 10 nm of a line perpendicular to the interface at the source metallurgical junction and within 10 nm of a similar line at the drain junction are tallied. The locations of these two electron populations in the Brillouin zone (BZ) are shown in **Figure 17**, for the source (a) and drain (b). The BZ is superposed on the data, with the positive k_x , k_y , and k_z axes shown in red, green, and blue,

respectively. Electron kinetic energies are indicated by color: Colors ranging from pure blue to red encode energies from 0 to 2.0 eV in 20 steps. The cold distribution at the source is indicated by the clear appearance of the six conduction-band minima (X valleys). The distribution at the drain is off-equilibrium, signified by the distribution throughout the BZ of the electrons. The drain field is directed in the $-k_x$ direction, which serves to shift the distribution along the $+k_x$ direction. Each image contains approximately 2000 particles.

The requirement for a Monte Carlo device model to predict MOSFET substrate and gate currents is a demanding one, and some progress on this problem has been made [71]. Still, the influence of the full band structure, electron-electron scattering, and plasma oscillations for this problem remain open. Preliminary results obtained with the DAMOCLES program indicate that such calculations are feasible but very expensive. To illustrate the ability to probe rare events, a 233-nm n-MOSFET was modeled at 300 K with $V_D = V_G =$ 2.5 V. The source and substrate are assumed to be grounded. To sample electronic behavior at energies sufficient to cause impact ionization (≥1.1 eV) or injection over the Si-SiO₂ barrier (≥3.1 eV), many statboxes must be defined. To this end, the channel is divided into 15 nonuniform intervals. Furthermore, each interval is subdivided into bins in kinetic energy, with a width of 0.2 eV. Thus, the ith stat-box has spatial thresholds $x_{L_i} \le x < x_{H_i}$ and energy thresholds $E_i \le E < E_i + 0.2$ (or, for the highest-energy box in each spatial interval, $E \ge E_i$). The highest-kinetic-energy enhancement threshold near the source is 1.0 eV, which increases to 3.4 eV toward the drain. Each individual stat-box is defined to nominally contain 44 electrons, and there are 182 such boxes. The statistical weight within each box is adjusted to maintain the target number of particles. A few comments are in order concerning this procedure. First, higher-energy particles are more expensive to process in the full band structure, as searches for final states must consider more bands. Second, subdividing distance and energy so finely raises the question of simply passing to the limit of infinitesimal divisions, and revamping the statistical weighting to populate uniformly with particles any space and/or energy regions of interest. This possibility must be traded off against the plethora of particle deletions and replications that will ensue in such a case, virtually undermining anything resembling a continuous particle trajectory. This occurs because very small (or infinitesimal) stat-boxes lower the probability of a particle covering a significant distance, as crossing into adjacent stat-boxes opens the possibility of conditionally removing the particle, should its statistical weight prove too small

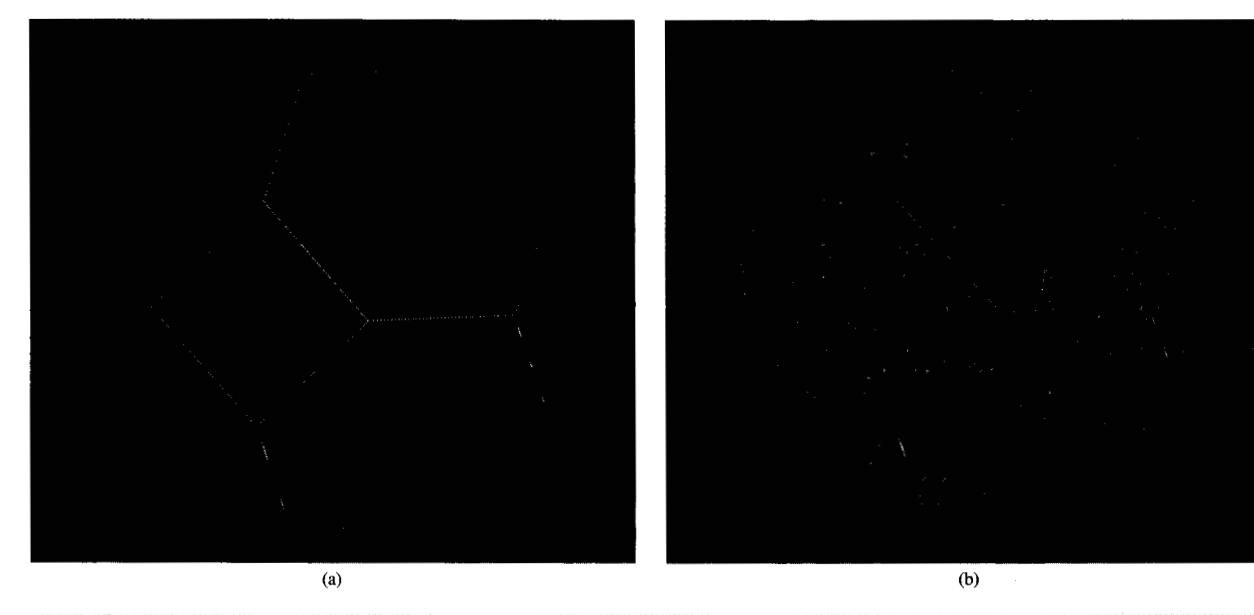




Flaure 16

Electron total energy distributions, calculated for a 53-nm-channel-length n-MOSFET at 77 K. Biases are assumed to be the same as for Figure 6(a). The 40 distributions stacked adjacent to one another are all normalized to have the same area. The same data are shown in (a) and (b), derived from opposite viewpoints.

locally. The quality of statistics that can be generated with many short-lived particles might then become questionable. Finally, enhancing rare events in a self-consistent potential forces more particles to be present in the model, because enough "common," low-energy particles must be present to accurately describe the charge density. The contradictory goals of populating both rare and common states, even with their different statistical weights, will raise the number of particles in the model and the cost of the computation. The results presented here are for non-self-consistent potentials only.



Picture 17

Calculated location of electrons in the Brillouin zone, sampled (a) within ± 10 nm of the source and (b) within ± 10 nm of the drain junctions, near the Si-SiO₂ interface. A 233-nm n-MOSFET at 300 K with $V_{\rm G}=V_{\rm D}=2.5$ V is considered. Electrons are colored according to their kinetic energy.

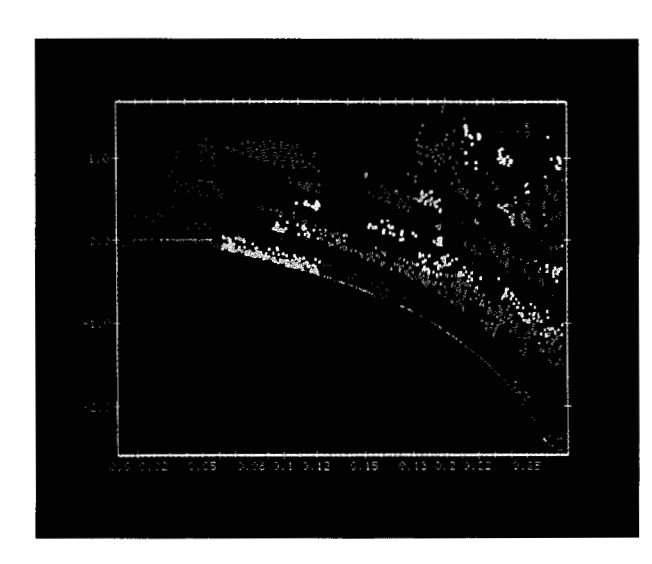


Figure 18

Electron total energy distribution in the channel, calculated for a 233-nm n-MOSFET at 300 K. It is assumed that $V_{\rm D}=V_{\rm G}=2.5$ V, and that source and substrate are grounded. Only electrons within 10 nm of the interface are shown. The electrons are colored according to their statistical weight, which ranges logarithmically from 2.8×10^6 to $1.1\times10^{-41}~{\rm cm}^{-1}$

Figure 18 shows the calculated channel potential together with the total electron energy distribution in the

channel at an instant in time. Only electrons within 10 nm of the interface are shown. The electrons are colored logarithmically according to their statistical weight (expressed as particles per electron per unit width). These weight factors range from 2.8×10^6 to 1.1×10^{-41} cm⁻¹, and span more than 47 orders of magnitude! While the physical accuracy of such a result has not been fully assessed (collective modes and short-range Coulombic forces are not included, and the statistical accuracy remains unclear), the robustness of the model is illustrated. The behavior of the electron distribution directly in the vicinity of the drain is of most interest, and is replotted in **Figure 19**.

In Figure 19(a) the total energy distribution of electrons within 10 nm of a line perpendicular to the interface at the drain junction is shown. Here, the zero of total energy represents the Fermi energy in the source of the MOSFET; the drain Fermi energy lies 2.5 eV below this. The inset shows the distribution on a linear scale. The contribution from a number of cold electrons is evident in the distribution, and results from the inclusion of a fraction of the drain in the sample space. Of central interest is the behavior of the heated part of the distribution, due to electrons moving in the channel. A displaced Maxwellian (DM) in total energy is also shown for comparison. The DM distribution function is usually expressed in terms of the wave vector **k** displaced from the origin by \mathbf{k}_0 as

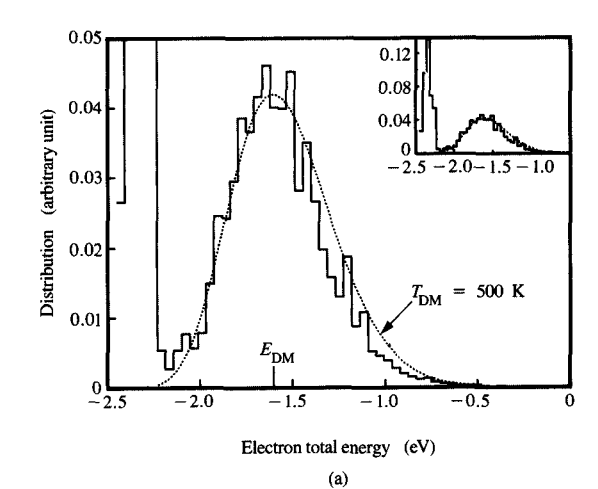
$$f_{\rm DM}(\mathbf{k}) \propto \exp\left(\frac{-\hbar^2 |\mathbf{k} - \mathbf{k}_0|^2}{2m^*k_{\rm B}T_{\rm DM}}\right),$$
 (6)

which applies in nondegenerate situations only. Assuming parabolic energy bands, and a displacement \mathbf{k}_0 in the k_x direction (due to the drain field), the function can be rewritten in terms of kinetic energy as

$$f_{\rm DM}(E) \propto \frac{k_{\rm B}T_{\rm DM}}{\sqrt{E_{\rm DM}}} \times \exp\left(-\frac{E + E_{\rm DM}}{k_{\rm B}T_{\rm DM}}\right)$$

$$\times \sinh\left(\frac{2\sqrt{EE_{\rm DM}}}{k_{\rm B}T_{\rm DM}}\right). \tag{7}$$

The kinetic energy $E_{\rm DM}$ is given by $E_{\rm DM}=\hbar^2k_{0x}^2/2m^*$. To plot this kinetic energy distribution on the total energy scale of Figure 19, zero kinetic energy is (somewhat arbitrarily) defined as coincident to the minimum total energy value. The distribution $f_{\rm DM}$ with $T_{\rm DM} = 500$ K and $E_{\rm DM} = 0.85 \text{ eV}$ is shown (note that $E_{\rm DM}$ is a kinetic energy, not a total energy, and hence is measured from the minimum total energy of the distribution function). It is difficult to give significance to $T_{\rm DM}$ and $E_{\rm DM}$, as this interval near the drain has a ~0.5-V drop in potential energy across it, complicating the mapping between total and kinetic energy. Furthermore, due to the effects of the full band structure, and possibly degeneracy, Equation (7) itself is not a rigorous result. Equation (7) is viewed as a fitting form only, with parameters E_{DM} and T_{DM} having little additional significance. Nevertheless, $E_{\rm DM}$ is the order of the local average kinetic energy near the drain, and $T_{\rm DM}$ gives a measure of the width of the distribution. The same results are plotted in Figure 19(b) on a logarithmic scale, to see the "hot tail" of the distribution. This DM fit remains credible up to -0.5 eV, where 0 eV is the Fermi energy in the source. The distribution falls more quickly above 0 eV and is well approximated by an exponential decay with an activation energy of 26 meV, i.e., the thermal energy. Further examination of the distribution near the source, and midway in the channel, shows that a marked decrease always occurs near 0 eV. However, the exponential slope beyond this knee in the curve appears to vary in the range 10-26 meV, although the results in this range are very noisy. This knee at ~0 eV in total energy has been observed previously, and has eluded simple explanation [75]. The distribution above 0 eV may be a replica of the thermal source distribution, but this is not certain. This knee seems related to the applied drain bias, but we find no reason why the temperature in the tail above 0 eV should approach the lattice temperature. The ultimate use of such distributions is in the calculation of quantities dependent on the hot tails, i.e., substrate and gate currents in MOSFETs, for example. Such work is in progress.



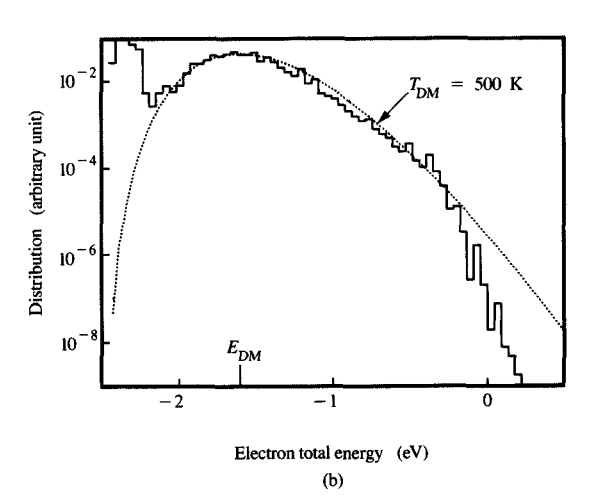
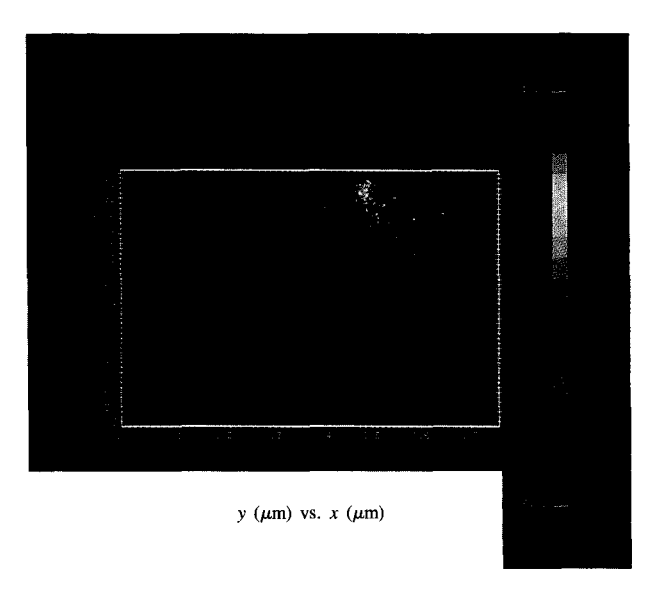


Figure 15

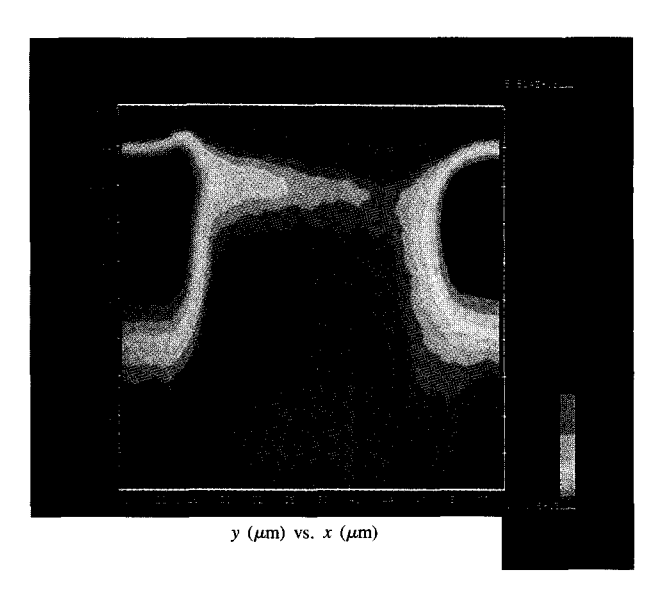
Calculated electron total energy distributions for the n-MOSFET of Figure 18, at T=300 K. The distribution is sampled within ± 10 nm of the drain metallurgical junction. The inset in (a) shows the entire distribution. The energetic portion of the distribution is enlarged in (a), and a displaced Maxwellian fit to this portion of the distribution is also shown. The same data, and the Maxwellian fit, are repeated in (b) on a logarithmic scale.

4. GaAs MESFET results

Results for a family of n-channel GaAs MESFETs, differing only in gate length, are described in this section. Because of the internal data structure of the DAMOCLES program, the switch from silicon to GaAs amounts to reading a different set of files describing the GaAs band structure and scattering rates. Thus, only the input parameters to the program need be changed to convert from a silicon to a GaAs device model. No separate, GaAs-only version of the program has been



Calculated electron distribution in the uppermost 0.5 μ m of a GaAs MESFET device domain, for $L_G = 0.25 \,\mu\text{m}$. The gate is assumed to extend from x = 0.25 to 0.50 μ m along the top surface. It is assumed that $V_{\rm G}=0.5$ V, $V_{\rm D}=1.0$ V, and T=300 K. Electrons are colored according to their kinetic energy.



Calculated electron distribution from Figure 20, represented as a contour plot. The channel region is magnified, which permits the density between source and drain to be clearly seen. The 20 contours range logarithmically from 10^{15} to 5.5×10^{18} cm⁻³.

created. A HEMT (high electron mobility transistor) could also be modeled, but without any real-space transfer of electrons into the AlGaAs layer

(heterostructures cannot at present be modeled by means of the DAMOCLES program).

The n-channel MESFETs considered here can be described as follows. The active layer is assumed to be uniformly doped at $N_D = 1.2 \times 10^{18} \text{ cm}^{-3}$ and is 25 nm thick. This active layer sits above an n layer doped $N_{\rm D} = 10^{14} \, {\rm cm}^{-3}$ which is 250 nm thick. Below this sits an undoped layer which is 250 nm thick, which rests finally on a p substrate doped $N_{\rm A} = 10^{16} {\rm cm}^{-3}$. For modeling, the first 1000 nm of the wafer below the surface is included, and a grounded ohmic back-side contact is defined. Source and drain are formed by the superposition of two Gaussian doping profiles, one donor type and one acceptor type, in order to approximate the compensation present in degenerately doped GaAs layers. These implants are self-aligned to the gate. The two Gaussians are given by

- $N_{\rm D,max} = 1.42 \times 10^{19} {\rm cm}^{-3}$, with a 14-nm straggle, peaked 27 nm below the surface. $N_{\rm A,max} = 1.12 \times 10^{19} {\rm cm}^{-3}$, with a 12.2-nm straggle,
- peaked 27 nm below the surface.

The model gate material is assumed to have a Schottky barrier height $\phi_{\rm B} = 0.7$ eV. To approximate Fermi-level pinning at a GaAs surface, a 5×10^{12} cm⁻² areal density of fixed negative charge is defined along the top surface of the device. All simulations are performed at 300 K, with electron-electron scattering included, and at a single bias point: $V_D = 1.0$ and $V_G = 0.5$ V. The behavior is compared for gate lengths L_G spanning the range $0.15-0.75 \mu m$.

Figure 20 shows the uppermost $0.5 \mu m$ of the MESFET device domain, for $L_G = 0.25 \mu m$. The gate extends from x = 0.25 to $0.50 \mu m$. The electron locations are shown at an instant in time, and their color reflects their kinetic energy. The kinetic energy ranges from 0 (blue) up to 1.0 eV (red) in 20 intervals. The degenerately doped source and drain are easily seen as elongated blue areas situated at $x \le 0.25$ and $x \ge 0.50 \mu m$. The surface depletion is clearly indicated, as is the depletion below the gate. The electrons are accelerated from left to right in the drain field, as is reflected in the kinetic energy gain. The active layer is only 250 Å thick $(0.975 \le y \le$ 1.0 µm), showing that hot electrons near the drain are injected into the buffer layer. The concentration of electrons for this same device is shown in Figure 21, and focuses on the region between source and drain and within 900 Å of the surface. The dominant electron flow occurs in the vicinity of the active layer-buffer layer interface ($y = 0.975 \mu m$), as can be seen. This is true for all the gate lengths considered here. For this reason, subsequent one-dimensional cuts through the device will consider a path along the active layer-buffer layer

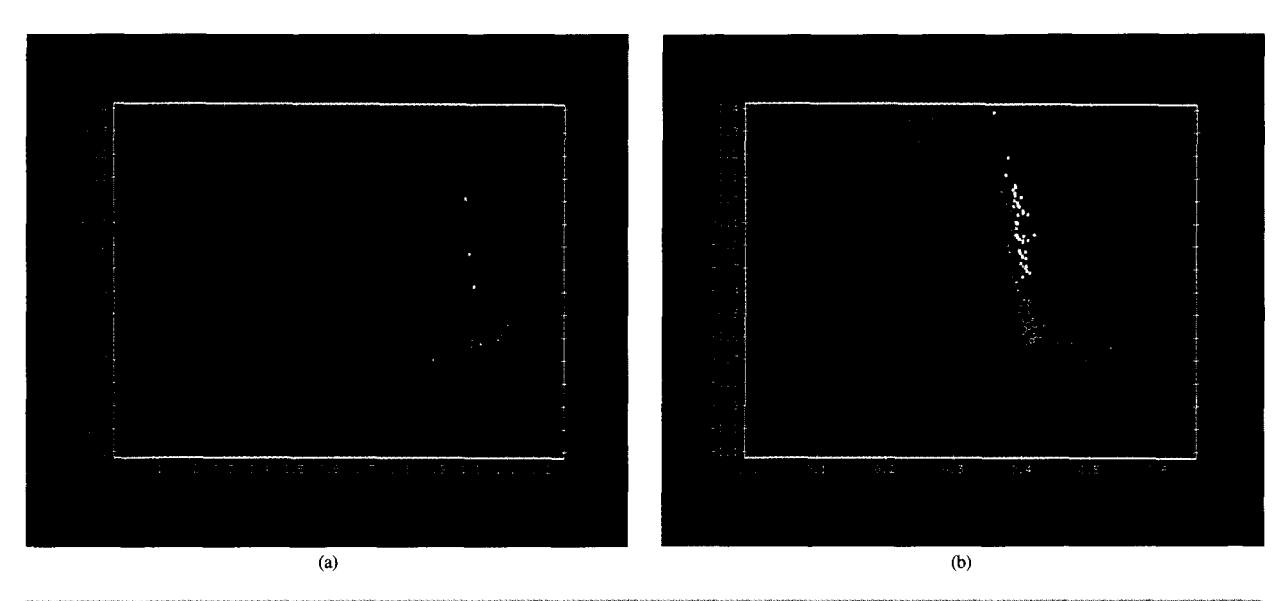


Figure 22

Calculated distribution in total energy of Monte Carlo electrons as a function of distance from source to drain for two MESFETs of differing gate length. In (a), results for a 0.75- μ m gate length are shown (gate spans 0.25-1.00 μ m); in (b), results for a 0.15- μ m gate length are shown (gate spans 0.25-0.40 μ m). The conduction-band energy is obtained along a line parallel to and 25 nm below the surface, and averaged over a width of ± 5 nm around this line. The distribution of electrons located within 5 nm of this same line is shown as well. The electrons are colored according to their location in the Brillouin zone.

interface (25 nm below the surface), with transverse spatial averaging extending ± 5 nm about this line in the y-axis direction.

In Figure 22 a comparison is made of the total energy of electrons versus position from source to drain at an instant in time, for the same bias conditions, for two different gate lengths. The conduction-band potential is obtained along the active layer-buffer layer interface with a ±5-nm transverse spatial average. The electrons shown are within 5 nm of the interface as well. Figure 22(a) shows results for a 0.75- μ m gate length (gate extends from 0.25 to 1.0 μ m), while Figure 22(b) shows those for a 0.15- μ m device (gate extends from 0.25 to 0.40 μ m). While the offset above the potential energy curve indicates the electron kinetic energy, the coloration of the electrons indicates their location in the BZ. Electrons in the Γ valley are blue, while electrons in the satellite valleys L and X are green and red, respectively. A few electrons, shown as white, are elsewhere in the BZ, and not readily associated with either Γ , L, or X. The source and drain are heavily doped, and this causes the L valleys to be occupied, even in equilibrium. Furthermore, through use of the DAMOCLES program, an increased average energy in the source and drain is predicted (approximately tens of meV per electron in this case) due to the Coulomb repulsion between point-like electrons immersed in a jellium doping. In [76], the complementary situation of point-like dopants in a

jellium of electrons is considered. In Figure 22(a), a moderate electric field exists over most of the channel, and the electrons come into local equilibrium with this field value. Only within the last 100 nm of the channel, near the drain, is nonequilibrium transport indicated. Here, carriers transfer from Γ to the satellite valleys (mostly L), as they enter the high-field region. An increased satellite valley population in the drain results, and the distance required to completely bleed off the excess L- and X-valley electrons appears to exceed the 0.25- μ m drain region of the model. In Figure 22(b), the same comments are true qualitatively concerning source and drain, but here strong off-equilibrium transport is seen over the length of the channel. The near-ballistic movement of electrons across the channel is signaled by the strong population near 0 eV total energy. Upon arriving at the drain, the hot electrons decay away, but again over a distance scale apparently exceeding 0.25 μ m.

In Figure 23, four internal distributions are shown as a function of position from source to drain, for four different gate lengths. The conduction-band potential is again obtained along the active layer-buffer layer interface with a ± 5 -nm transverse spatial average, and the electrons shown are within 5 nm of the interface. The bias conditions are the same as used previously. The gate lengths considered are $L_{\rm G}=0.15,\,0.25,\,0.50,\,{\rm and}\,0.75$ μm . The four variables plotted are (a) electron energy, (b) electric field, (c) electron velocity, and (d) electron

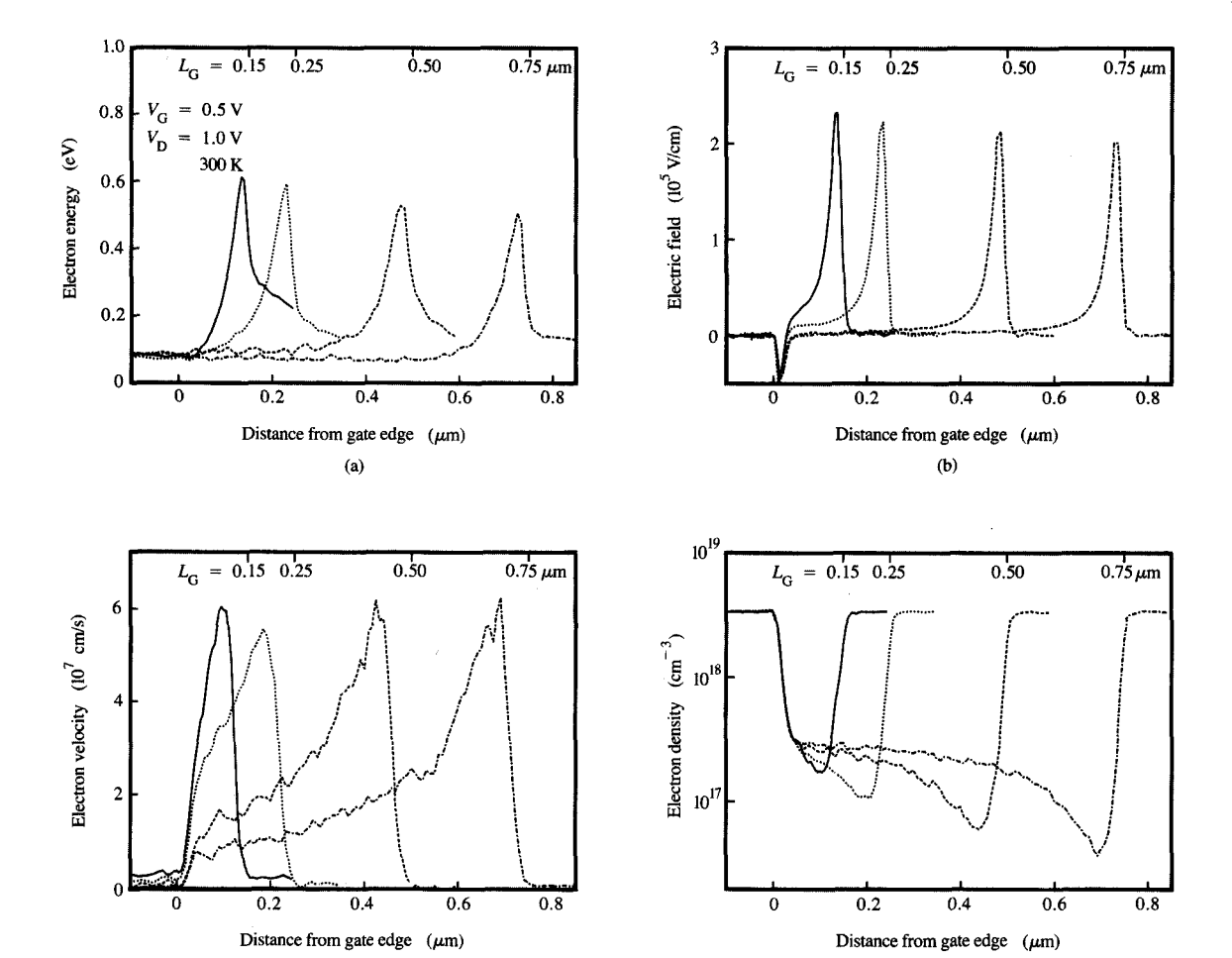


Figure 23

(a) Electron energy, (b) electric field, (c) electron velocity, and (d) electron density from source to drain calculated for four MESFETs of differing gate lengths, at $T=300~\rm K$. The gate lengths considered are $L_{\rm G}=0.15,\,0.25,\,0.50,\,$ and $0.75~\mu \rm m$. It is assumed that $V_{\rm G}=0.5~\rm V,\,V_{\rm D}=1.0~\rm V,\,$ and that sources and substrates are grounded.

density. In part (a), the electron energy peaks near the drain edge of the gate and extends backward toward the source, as well as into the drain. This region of high energy nominally covers a distance of $\sim 0.1~\mu m$, with the balance of the channel assuming near-thermal energy values, especially for the longer gate lengths. The curves are terminated $0.1~\mu m$ past the gate edge in each direction; hence, the decay of hot carriers in the drain is not fully indicated here. In part (b), the electric field in the drain–source direction is plotted. The field peaks near the drain end of the gate, very near where the energy peaks. The shape of the field in the channel is qualitatively similar to the shape of the energy, except for

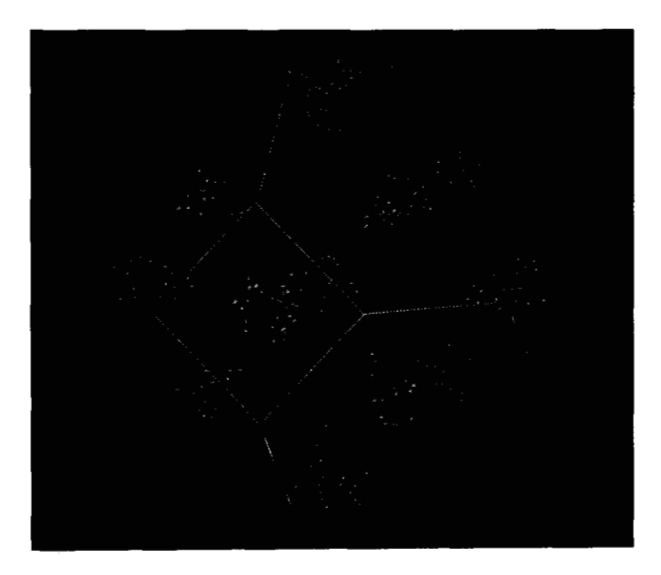
(c)

the smallest gate lengths, where a significant field reaches all the way back toward the source, even though the energy remains low there. In the drain, the field drops abruptly, but the energy cannot relax so quickly. In part (c), the velocity of electrons in the channel is shown. Peak velocities are high, and point to strong velocity overshoot in the high field near the drain. In the channel, the velocity increases as the channel becomes shorter, with off-equilibrium behavior consuming the entire channel at 0.15-µm gate length. Note that the velocity peak occurs farther from the drain than the energy or field peaks, as expected with velocity overshoot. As the energy rises and the scattering rate increases in concert,

(d)

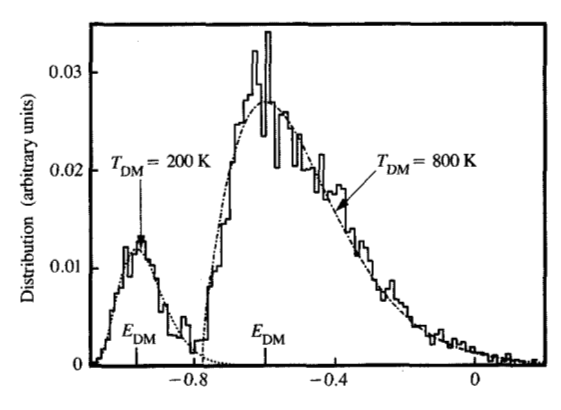
the velocity quickly peaks due to the increased backscattering of electrons. Furthermore, transferring from Γ to the satellite valleys becomes feasible when the kinetic energy exceeds ~0.3 or ~0.45 eV (for transfer to L or X, respectively). This additional scattering contributes to separating the locations of the peak velocity and energy. The correlation between the location of the peak channel velocity and the onset of scattering to the satellite valleys can be easily verified. Referring back to Figure 22, in both parts (a) and (b) the potential has a distinct knee, where a lower channel field increases abruptly as the drain is approached. This knee occurs when the potential energy equals ~-0.3 eV relative to the source Fermi energy. From this point on in the channel, transfer to L (and shortly thereafter, X) can commence. The location of this knee is virtually the location of the velocity maximum seen in Figure 23(c). Note that the time to transfer from Γ to the satellite valleys is very short, <100 fs, which translates into $<0.05 \mu m$ at a velocity of 5×10^7 cm/s. From Figure 23(a, b), the energy and field peaks are at nearly identical positions, located $\sim 0.035 \, \mu \text{m}$ downstream from the respective velocity peaks. The transit times computed from the four velocity characteristics of Figure 23(c) are 0.44, 0.92, 2.8, and 5.5 ps, for the smallest to largest device. This is the time needed to traverse the distance under the gate, minus a fixed distance of 0.015 μ m taken off each end of the gate, to avoid including the source/ drain regions beneath the gate. The corresponding transit velocities over the distance ($L_G - 0.03 \mu m$) are 2.7, 2.4, 1.7, and 1.3×10^7 cm/s. The electron density, shown in Figure 23(d), generally decreases from source to drain in response to the increase in velocity down the channel. The sharp pinch-off behavior at the longest gate lengths is smeared out in the smaller devices.

Finally, two plots related to quantifying the electron distribution in the MESFET channel are offered. Figure 24 shows the BZ of GaAs and contains the calculated electron kinetic energy distribution at an instant in time present in a 0.15-µm-gate-length MESFET near the drain end of the channel. Only electrons within ±10 nm of the drain end of the gate (at any depth below the interface) are shown. The electrons are colored according to kinetic energy, ranging from 0 (blue) to 1.0 eV (red). The electrons are also depth-cued, rendering electrons farther in the back in progressively duller colors. The grouping at the Γ valley (origin), the eight L valleys, and the six X valleys can all be discerned. The drain field shifts the distribution in the $+k_r$ (red) axis direction. Note the relatively cool populations at the X points along $\pm k_{,,}$ owing to the low energies associated with the constriction of electron movement perpendicular to the surface of the MESFET. For the X valleys along $\pm k_z$, however,



Faure 24

Calculated location of electrons in the GaAs Brillouin zone, sampled within ± 10 nm of the drain end of the gate in a 0.15- μ m-gate-length MESFET, at T=300 K. Assumed biases are $V_{\rm G}=0.5$ V and $V_{\rm D}=1.0$ V. Electrons are colored according to their kinetic energy.



Electron total energy (eV)

Figure 2

Electron energy distribution from Figure 24, replotted as a distribution in total energy. A displaced Maxwellian function is fitted to each portion of the distribution.

the out-of-plane direction presents no such confinement, and hotter electrons can be seen as a result.

In Figure 25, the same data shown in Figure 24 are replotted as a distribution in total energy. Here, the zero

of total energy represents the Fermi energy in the source of the MESFET; the drain Fermi energy lies 1.0 eV below this, and the conduction-band edge ~100 meV lower still due to degeneracy in the drain. The distribution is a mixture of Γ -, L-, and X-valley electrons. The Γ -valley electrons are easily sorted out by virtue of their lower energy, and reflect the presence of the drain in the sample space. Thus, most of these electrons have not traveled across the channel. The higher-energy population is a mixture of L- and X-valley electrons which have entered the drain after crossing the channel. The average total energy of the entire distribution is -0.56 eV. Two displacement Maxwellians in energy [Equation (7)] are fitted to the two prominent portions of the distribution, as shown in Figure 25. The fit is good, but as discussed earlier, too much importance should not be attributed to the energy offsets (E_{DM}) or effective temperatures (T_{DM}) . This is underscored by the apparently anomalous value of $T_{\rm DM} = 200~{\rm K}$ for the Γ-valley electrons. Rather, a DM distribution does not describe the degenerately doped drain distribution correctly, rendering the quantities E_{DM} and T_{DM} merely fitting parameters. For the satellite valley distribution, the full band structure, together with the admixture of L and X valleys, undermines the physical correctness of a DM description. However, as a general fitting form, with just two parameters, the DM form does track the shape of the distribution quite well.

5. Si bipolar transistor results

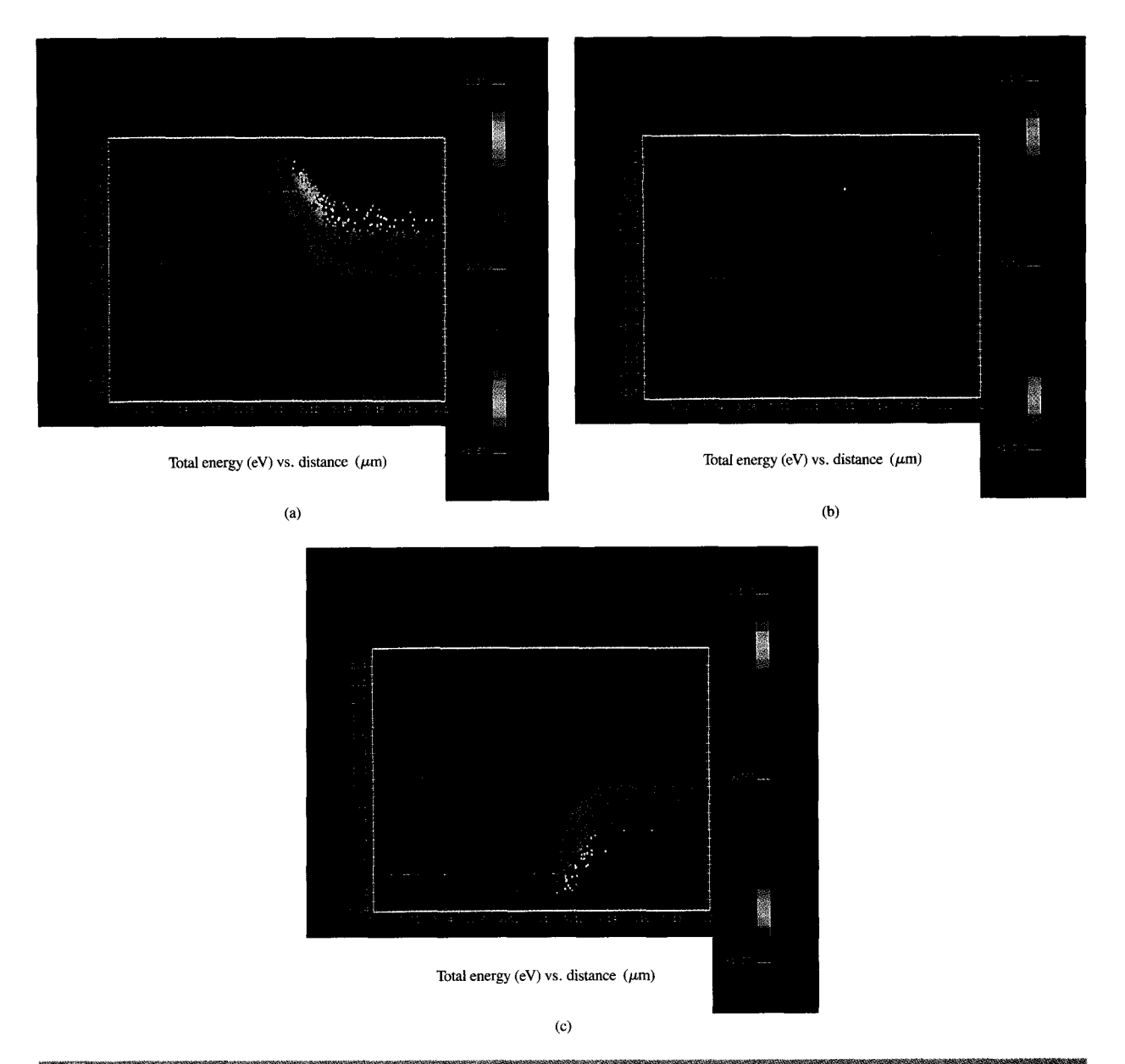
The enhancements to the DAMOCLES program to permit bipolar transistor simulation are quite unique: This is the first Monte Carlo device model for a bipolar transistor in which Monte Carlo electrons and holes are included, both in their respective band structures. To demonstrate our approach, a model bipolar transistor geometry is simulated. The transistor domain is assumed to be a rectangle $0 \le x \le 200$ nm and $0 \le y \le 100$ nm. The doping profile for the npn transistor is assumed to be piecewise constant:

- Emitter, $N_D = 1.0 \times 10^{19} \text{ cm}^{-3} \text{ for } x < 50 \text{ nm.}$ Base, $N_D = 1.0 \times 10^{18} \text{ cm}^{-3} \text{ and } N_A = 4.0 \times 10^{18} \text{ cm}^{-3}$ for 50 < x < 100 nm.
- Collector, $N_D = 1.0 \times 10^{18} \text{ cm}^{-3} \text{ for } x > 100 \text{ nm}.$

Other assumptions are as follows: The metallurgical emitter and base widths are 50 nm, and the collector is 100 nm long; the emitter and collector contacts cover the vertical height of the domain, $0 \le y \le 100$ nm, at opposite ends of the model; and the base contact lies along the top edge, y = 100 nm, and covers $61.2 \le x$ \leq 81.6 nm in the horizontal direction. The base contact collects large quantities of electrons emitted over the

base-emitter barrier, due to the lack of an extrinsic base region. As a result, this model structure is useless in predicting current gain; however, the velocities and energies of carriers crossing the base-collector depletion region are considered representative. A complementary, but otherwise identical, pnp transistor structure is modeled as well, to provide a comparison between the transport properties of electrons and holes. The npn (pnp) device bias is $V_{\rm BF} = 0.9 \, (-0.9)$ and $V_{\rm CF} = 1.5$ (-1.5) V. Unless otherwise specified, particle-particle scattering is in effect for these simulations.

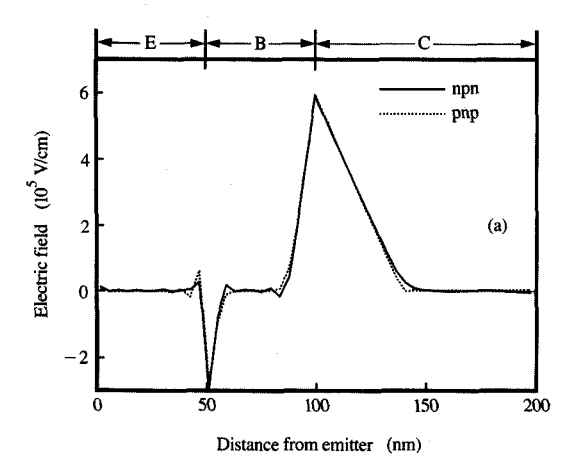
In Figure 26(a) the calculated total energy distribution at an instant in time is plotted against the distance from the emitter to the collector for the npn transistor. Both conduction and valence band edges are seen as cyan curves. The Monte Carlo electrons and holes are also shown projected onto the potential energy curves. Electron potential energy increases upward, while hole potential energy increases downward. The carrier kinetic energy is indicated by the color of the particles, with blue denoting 0 and red denoting 1.5 eV, in 20 steps. The electron flux from the emitter, across the base, and into the collector is clearly seen. Thermal holes are present in the base, with some modest level of backward injection of holes into the emitter. The heating of electrons as they enter the high field in the base-collector depletion region is well represented. In order to sample the behavior of electrons at such energies in the depletion region, statboxes must be employed. Here, the population of the tail of the distribution in the emitter is increased with statboxes, providing a significant number of electrons with energies large enough to surmount the emitter-base barrier. Then, these rare electrons are followed through the base and the base-collector depletion region. Finally, stat-boxes in the collector provide a balanced mix between the flux of hot electrons entering the collector and the thermal electrons in the charge neutral collector. If electrons and holes had the same statistical weight, i.e., if there were no stat-boxes, the bipolar device would appear as in Figure 26(b). Here, the relative distributions in energy and space may be compared throughout the entire device without regard to variations in the statistical weight of individual particles. However, to obtain accurate statistics describing electron behavior in the base-collector depletion region would require inordinate amounts of computing time. In Figure 26(c), the pnp result complementary to Figure 26(a) is shown. The hole flux from emitter to collector is amplified in a manner similar to the treatment for electrons in the npn transistor. The kinetic energy is shown with the same color scale here, indicating that hot holes are somewhat cooler than their electron counterparts in Figure 26(a). This occurs because of the higher scattering rates for holes and their resultant shorter mean free paths between scattering events.

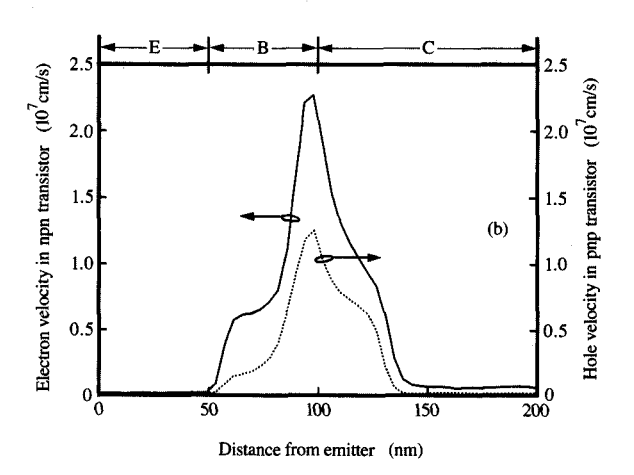


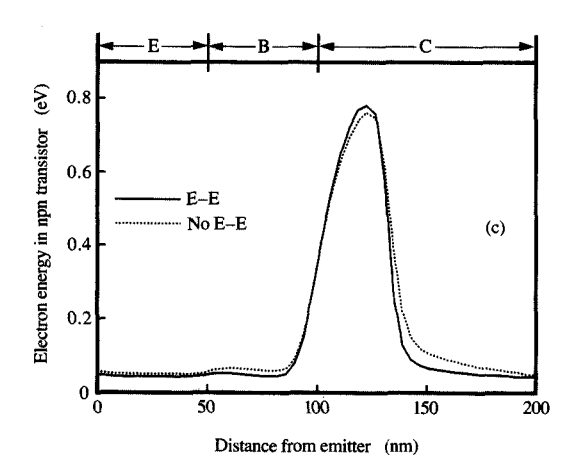
Calculated distribution in total energy of the Monte Carlo electrons and holes for two complementary silicon bipolar transistors versus the distance from the emitter to the collector. Results for the npn transistor are shown in (a) and (b), with $V_{\rm BE}=0.9~{\rm V}$ and $V_{\rm CE}=1.5~{\rm V}$. Results for the pnp transistor are shown in (c), with $V_{\rm BE}=0.9~{\rm V}$ and $V_{\rm CE}=1.5~{\rm V}$. The carrier flux from emitter to collector is evident in (a) and (c) due to the use of stat-boxes. Carriers are colored according to their kinetic energy.

The electric fields present in the npn and pnp complementary pair are virtually identical (ignoring the factor of -1), as can be seen in Figure 27(a). The peak field at the emitter-base barrier is $\sim 3 \times 10^5$ V/cm in magnitude, while the peak field in the base-collector depletion region reaches nearly twice this value. Such high fields in the collector result in both velocity overshoot and the possibility of impact ionization. In

Figure 27(b), the electron velocity in the npn device is compared to the hole velocity in the pnp transistor, both as a function of distance from the emitter. The velocity shows the same qualitative features for the npn and pnp transistors. The velocity levels off in the charge-neutral part of the base. For the npn transistor, this electron velocity approaches 0.7×10^7 cm/s, while for the pnp transistor this hole velocity reaches only 0.15×10^7 cm/s.







(a) Calculated electric field and (b) carrier velocity versus distance from emitter to collector, for the complementary npn and pnp bipolar transistors of Figure 26. In (c), the electron kinetic energy for the npn transistor is shown; the result shows slight dependence on the presence of carrier-carrier scattering, abbreviated by "E-E."

The velocity of the carriers increases rapidly as they leave the neutral part of the base. The peak velocity is obtained just inside the metallurgical base near the base-collector junction, with values of 2.27×10^7 and 1.25×10^7 cm/s for electrons and holes, respectively. The velocity then decreases as the energy of the carriers increases. The velocity should decay down to the saturated velocity; however, this trend is masked by the decreasing field magnitude as the neutral collector is approached. Finally, the onset of the neutral collector causes the average velocity to drop abruptly near 135 nm. The time required to cross the neutral base and the depletion region (from 60 to 135 nm in the figure) is 0.86 and 2.3 ps for the npn and pnp transistors, respectively. Figure 27(c) shows the kinetic energy of electrons in the npn transistor for the cases of particle-particle scattering included in and removed from the calculation (here the figure caption "E-E" implies all possible bipolar interactions: e-e, e-h. and h-h). The energy peaks farther toward the collector than the velocity, which is the typical velocity overshoot behavior. Neglecting particle-particle scattering changes the picture subtly. Perhaps most noticeable is the slower decay of the energy in the collector without particleparticle scattering. It is hypothesized that particle-particle scattering, although preserving the total kinetic energy of the interacting particles (and hence unable to alter the average energy), can backscatter hot carriers, giving them more opportunity to lose energy to phonons. This results in a more effective energy-dissipation mechanism. The hole energy in the pnp transistor is analogous to that in Figure 27(c), except that the peak energy reaches only 0.5 eV. Preliminary results indicate somewhat less sensitivity of the kinetic energy to particle-particle scattering in the pnp case. Further work is required to understand this behavior.

For a bipolar simulation, impact ionization and the subsequent generation of an electron-hole pair is explicitly included. To demonstrate this, consider the npn transistor described previously, but with the collector voltage increased to $V_{\rm CE} = 2.5$ V. The creation of electron-hole pairs by energetic electrons moving across the depletion region becomes easy to observe at 2.5 V, for the same stat-box definitions as used in the 1.5-V collector bias case. Figure 28 shows a portion of a total energy distribution versus distance at an instant in time for this situation, with the central focus being the trajectory of a hole generated by impact ionization. The hole trajectory is projected onto this one-dimensional distance scale; hence, movement in the out-of-plane direction is not indicated. The hole was created in the base-collector depletion region at 0.122 μ m, with an initial kinetic energy of ~ 0.7 eV. Immediately, this hole moves toward the base in response to the field. The hole scatters in the process, with each scattering event

indicated by an ×. The emission of phonons, both optical and acoustic, represents the bulk of the scatterings portrayed here. Although not shown, the hole ultimately thermalizes in the base. The trajectory shown contains a few discontinuities in the total energy not associated with any scattering. This is only an artifact of the plotting procedure, and is due to the failure to correct for the time-varying character of the self-consistent potential energy over the time interval spanned by the trajectory (in this case, just under 0.2 ps). Clearly, the DAMOCLES program demonstrates the rigor necessary to track the products of impact ionization. This should allow insight into the overall process of optimizing the collector doping for high-speed silicon bipolar transistors.

6. Concluding remarks

The DAMOCLES program provides a flexible and powerful means for carrying out Monte Carlo simulation of the behavior of semiconductor devices. The completeness of the physical description, together with its applicability to the treatment of a wide class of device structures, represents a unique simulation capability. Our goal is to construct a program which can form a reference against which other, less computation-consuming, device models can be calibrated and compared. Such comparisons, both theoretical and experimental, are ongoing.

Perhaps most frustrating from today's vantage point is the amount of computer time required to generate useful results with the DAMOCLES program. Our ability to characterize our model is gated by our computation requirements. Execution times span 2-100 CPU seconds/ (particle × ps). That is, on a uniprocessor IBM 3090S with a vector facility, the DAMOCLES program requires 2-100 CPU seconds to advance one particle (electron or hole) one picosecond in simulation time. About 50% of the computation time is spent executing vector hardware instructions. Typical runs track 5000-10000 particles for 3-5 ps, assuming a rate of ~5 CPU seconds/(particle × ps). The CPU time required depends on the energy of the carriers present (hotter carriers require searches over more bands to find final states), the frequency of the Poisson solution, and whether particle-particle scattering is included. Recent work indicates that the particleparticle scattering algorithm employed can be implemented on a 3090 in parallel with excellent processor utilization [77]. However, this represents at most only a sixfold decrease in elapsed time for the calculation. Our hope is that massively parallel computing architectures will make it possible to more effectively use the DAMOCLES program by dramatically cutting the elapsed time for a single calculation.

Finally, more physical phenomena could be incorporated into the DAMOCLES program. Our

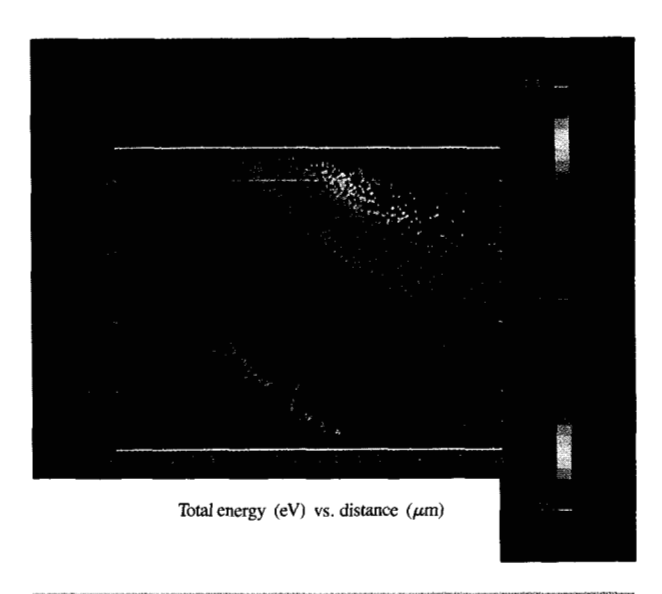


Figure 28

Calculated distribution in total energy of the Monte Carlo electrons and holes for the transistor of Figure 26(a), except that $V_{\rm CE}=2.5$ V. The plot is centered around the base–collector depletion region in order to show the trajectory in total energy of a single hole (green line) created by impact ionization. The hole scatters as it moves toward the base, and each scattering event is indicated by an \times .

simulations are currently limited to single-crystal semiconductor devices; however, work is already underway toward extending the program, with its full band structure paradigm intact, to GaAs-AlGaAs and Si-Ge heterojunction device simulation. In addition, our treatment of inversion layers to date has not taken quantization effects into account. Although this appears reasonable for sufficiently hot carriers in the channel, our ultimate goal is to merge 2D quantization effects for inversion layers with the present treatment of bulk transport, respecting the full band structure of the crystal in every case. Such additional function will, unfortunately, cause associated computational requirements to increase.

Acknowledgments

We are particularly indebted to R. Car for providing the kernel of the pseudopotential band-structure calculation. We also acknowledge W. Lee for his ongoing interest in bipolar device simulations with the DAMOCLES program, A. Fowler, P. Price, C. Jacoboni, F. Stern, and A. Williams (now with Thinking Machines Incorporated, Cambridge, MA) for discussions and managerial support, and J. Wells, W. Pope, R. Kenneson, R. McNeill, L. Lin, A. Zlatsin, and the entire Multiple Virtual Storage staff for computing support at both the IBM Yorktown and Hawthorne sites. We are indebted to C. Pickover for

Figures 17 and 24, which were rendered on a Stellar GS1000* graphic supercomputer.

References and notes

- A. DiMari, "An Accurate Numerical Steady-State One-Dimensional Solution of the P-N Junction," Solid-State Electron. 11, No. 1, 33–58 (1968).
- A. DiMari, "An Accurate Numerical One-Dimensional Solution of the P-N Junction Under Arbitrary Transient Conditions," Solid-State Electron. 11, No. 11, 1021–1053 (1968).
- D. L. Scharfetter and H. K. Gummel, "Large-Signal Analysis of a Silicon Read Diode Oscillator," *IEEE Trans. Electron Devices* ED-16, No. 1, 64-77 (1969).
- D. P. Kennedy and R. R. O'Brien, "Computer Aided Two-Dimensional Analysis of the Junction Field-Effect Transistor," IBM J. Res. Develop. 14, No. 2, 95-116 (1970).
- D. P. Kennedy and P. C. Murley, "Steady State Mathematical Theory for the Insulated Gate Field Effect Transistor," *IBM J. Res. Develop.* 17, No. 1, 2-12 (1973).
- J. W. Slotboom, "Computer-Aided Two-Dimensional Analysis of Bipolar Transistors," *IEEE Trans. Electron Devices* ED-20, No. 8, 669-679 (1973).
- P. E. Cottrell and E. M. Buturla, "Steady State Analysis of Field Effect Transistors via the Finite Element Method," *Proceedings* of the 1975 IEEE International Electron Devices Meeting, Washington, DC, 1975, pp. 51–54.
- W. VanRoosbroeck, "Theory of the Flow of Electrons and Holes in Germanium and Other Semiconductors," *Bell Syst. Tech. J.* 29, No. 10, 560–607 (1950).
- S. Selberherr, Analysis and Simulation of Semiconductor Devices, Springer-Verlag, Vienna, 1984.
- P. Rohr, F. A. Lindholm, and K. R. Allen, "Questionability of Drift-Diffusion Transport in the Analysis of Small Semiconductor Devices," *Solid-State Electron.* 17, No. 7, 729– 734 (1974).
- J. R. Barker and D. K. Ferry, "On the Physics and Modeling of Small Semiconductor Devices—I," *Solid-State Electron.* 23, No. 6, 519–530 (1980).
- T. Toyabe, H. Masuda, Y. Aoki, H. Shukuri, and T. Hagiwara, IEEE Trans. Electron Devices ED-32, No. 10, 2038–2044 (1985)
- N. Shigyo, S. Fukuda, T. Wada, K. Hieda, T. Hamamoto, H. Watanabe, K. Sunouchi, and H. Tango, "Three-Dimensional Analysis of Subthreshold Swing and Transconductance for Fully Recessed Oxide (Trench) Isolated 1/4-µm-Width MOSFET's," IEEE Trans. Electron Devices 35, No. 7, 945-951 (1988).
- E. M. Buturla, P. E. Cottrell, B. M. Grossman, and K. A. Salsburg, "Finite-Element Analysis of Semiconductor Devices: The FIELDAY Program," *IBM J. Res. Develop.* 25, No. 4, 218–231 (1981).
- Personal communication, S. Selberherr, Technical University of Vienna, Austria, March 1989.
- B. Carnez, A. Cappy, A. Kaszynski, E. Constant, and G. Salmer, "Modeling of a Submicrometer Gate Field-Effect Transistor Including Effects of Nonstationary Electron Transport," J. Appl. Phys. 51, No. 1, 784-790 (1980).
- 17. W. R. Curtis and Y.-H. Yun, "A Temperature Model for the GaAs MESFET," *IEEE Trans. Electron Devices* **ED-28**, No. 8, 954–962 (1981).
- R. K. Cook and J. Frey, "An Efficient Technique for Two-Dimensional Simulation of Velocity Overshoot Effects in Si and GaAs Devices," COMPEL 1, No. 2, 65-87 (1982).
- T. Kobayashi and K. Saito, "Two-Dimensional Analysis of Velocity Overshoot Effects in Ultrashort-Channel Si MOSFET's," *IEEE Trans. Electron Devices* ED-32, No. 4, 788–792 (1985).
- D. J. Widiger, I. C. Kizilyalli, K. Hess, and J. J. Coleman, "Two-Dimensional Transient Simulation of an Idealized High

- Electron Mobility Transistor," *IEEE Trans. Electron Devices* **ED-32**, No. 6, 1092–1102 (1985).
- J. F. Palmier, J. Dangla, E. Caquot, and M. Campana, "Numerical Simulation of Electrical Transport in III-V Microstructure Devices," Proceedings of the Fourth International Conference on Numerical Analysis of Semiconductor Devices and Integrated Circuits (NASECODE IV), J. J. H. Miller, Ed., Boole Press, Dublin, Ireland, 1985, pp. 70-82.
- I. C. Kizilyalli, K. Hess, J. L. Larson, and D. J. Widiger, "Scaling Properties of High Electron Mobility Transistors," *IEEE Trans. Electron Devices* ED-33, No. 10, 1427–1433 (1986).
- 23. C. M. Snowden and D. Loret, "Two-Dimensional Hot-Electron Models for Short-Gate-Length GaAs MESFET's," *IEEE Trans. Electron Devices* ED-34, No. 2, 212–223 (1987).
- M. Fukuma and W. W. Lui, "MOSFET Substrate Current Model Including Energy Transport," *IEEE Electron Device Lett.* EDL-8, No. 5, 214–216 (1987).
- W. Hänsch and S. Selberherr, "MINIMOS 3: A MOSFET Simulator that Includes Energy Balance," *IEEE Trans. Electron Devices* ED-34, No. 5, 1074–1078 (1987).
- H.-H. Ou and T.-W. Tang, "Numerical Modeling of Hot Carriers in Submicrometer Silicon BJT's," *IEEE Trans. Electron Devices* ED-34, No. 7, 1533–1539 (1987).
- 27. R. Stenzel, H. Elschner, and R. Spallek, "Numerical Simulation of GaAs MESFETs Including Velocity Overshoot," *Solid-State Electron.* **30**, No. 8, 873–877 (1987).
- C. L. Wilson, "Hydrodynamic Carrier Transport in Semiconductors with Multiple Band Minima," *IEEE Trans. Electron Devices* 35, No. 2, 180–187 (1988).
- A. Forghieri, R. Guerrieri, P. Ciampolini, A. Gnudi, M. Rudan, and G. Baccarani, "A New Discretization Strategy of the Semiconductor Equations Comprising Momentum and Energy Balance," *IEEE Trans. Computer-Aided Design* 7, No. 2, 231– 242 (1988)
- B. Meinerzhagen and W. L. Engl, "The Influence of the Thermal Equilibrium Approximation on the Accuracy of Classical Two-Dimensional Numerical Modeling of Silicon Submicron MOS Transistors," *IEEE Trans. Electron Devices* 35, No. 5, 689-697 (1988).
- 31. Y. Feng and A. Hintz, "Simulation of Submicron GaAs MESFET's Using a Full Dynamic Transport Model," *IEEE Trans. Electron Devices* 35, No. 9, 1419-1431 (1988).
- E. M. Azoff, "Energy Transport Numerical Simulation of Graded AlGaAs/GaAs Heterojunction Bipolar Transistors," IEEE Trans. Electron Devices 36, No. 4, 609-616 (1989).
- K. Horio, Y. Iwatsu, and H. Yanai, "Numerical Simulation of AlGaAs/GaAs Heterojunction Bipolar Transistors with Various Collector Parameters," *IEEE Trans. Electron Devices* 36, No. 4, 617–624 (1989).
- R. W. Hockney and R. A. Warriner, "Two-Dimensional Particle Models in Semiconductor-Device Analysis," *Electron. Lett.* 10, No. 23, 484–486 (1974).
- G. Baccarani, C. Jacoboni, and A. M. Mazzone, "Current Transport in Narrow-Base Transistors," Solid-State Electron. 20, No. 1, 5-10 (1977).
- J.-F. Pone, R. C. Castagné, J.-P. Courat, and C. Arnodo, "Two-Dimensional Particle Modeling of Submicrometer Gate GaAs FET's Near Pinchoff," *IEEE Trans. Electron Devices* ED-29, No. 8, 1244–1255 (1982).
- 37. H. L. Grubin, J. P. Kreskovsky, G. J. Iafrate, D. K. Ferry, and R. F. Greene, "Physics and Modeling Considerations for VLSI Devices," *The Physics of Submicron Structures*, H. Grubin, K. Hess, G. Iafrate, and D. Ferry, Eds., Plenum Press, New York, 1984, pp. 63–75.
- 38. R. Fauquembergue, M. Pernisek, and E. Constant, "Monte Carlo Simulation of Space-Charge Injection FET," *The Physics of Submicron Structures*, H. Grubin, K. Hess, G. Iafrate, and D. Ferry, Eds., Plenum Press, New York, 1984, pp. 171-176.
- Y.-J. Park, D. H. Navon, and T.-W. Tang, "Monte Carlo Simulation of Bipolar Transistors," *IEEE Trans. Electron Devices* ED-31, No. 12, 1724–1730 (1984).

492

^{*} Stellar and GS1000 are trademarks of Stellar Computer, Inc., Newton, MA.

- P. T. Nguyen, D. H. Navon, and T.-W. Tang, "Boundary Conditions in Regional Monte Carlo Device Analysis," *IEEE Trans. Electron Devices* ED-32, No. 4, 783–787 (1985).
- M. Tomizawa, A. Yoshii, and K. Yokoyama, "Modeling for an AlGaAs/GaAs Heterostructure Device Using Monte Carlo Simulation," *IEEE Trans. Electron Device Lett.* EDL-6, No. 7, 332-334 (1985).
- K. Tomizawa and H. Hashizume, "Method of Monte Carlo Simulation for Submicron Heterojunction Devices," Proceedings of the Fourth International Conference on Numerical Analysis of Semiconductor Devices and Integrated Circuits (NASECODE IV), J. J. H. Miller, Ed., Boole Press, Dublin, Ireland, 1985, pp. 98–107.
- P. Hesto, J.-F. Pone, M. Mouis, J.-L. Pelouard, and R. Castagné, "Monte-Carlo Modelling of Semiconductor Device," Proceedings of the Fourth International Conference on Numerical Analysis of Semiconductor Devices and Integrated Circuits (NASECODE IV), J. J. H. Miller, Ed., Boole Press, Dublin, Ireland, 1985, pp. 315–319.
- K. Yokoyama, M. Tomizawa, and A. Yoshii, "Scaled Performance for Submicron GaAs MESFET's," *IEEE Trans. Electron Device Lett.* EDL-6, No. 10, 536-538 (1985).
- T. Wang and K. Hess, "Calculation of the Electron Velocity Distribution in High Electron Mobility Transistors Using an Ensemble Monte Carlo Method," J. Appl. Phys. 57, No. 12, 5336-5339 (1985).
- C. Moglestue, "A Self-Consistent Monte Carlo Particle Model to Analyze Semiconductor Microcomponents of Any Geometry," *IEEE Trans. Computer-Aided Design* CAD-5, No. 2, 326–345 (1986).
- U. Ravaioli and D. K. Ferry, "MODFET Ensemble Monte Carlo Model Including the Quasi-Two-Dimensional Electron Gas," *IEEE Trans. Electron Devices* ED-33, No. 5, 677–681 (1986).
- C. M. Maziar, M. E. Klausmeier-Brown, S. Bandyopadhyay, M. S. Lundstrom, and S. Datta, "Monte Carlo Evaluation of Electron Transport in Heterojunction Bipolar Transistor Base Structures," *IEEE Trans. Electron Devices* ED-33, No. 7, 881– 888 (1986).
- K. Throngnumchai, K. Asada, and T. Sugano, "Modeling of 0.1-μm MOSFET on SOI Structure Using Monte Carlo Simulation Technique," *IEEE Trans. Electron Devices* ED-33, No. 7, 1005-1011 (1986).
- Y. Awano, M. Kosugi, T. Mimura, and M. Abe, "Performance of a Quarter-Micron-Gate Ballistic Electron HEMT," *IEEE Electron Device Lett.* EDL-8, No. 10, 451–453 (1987).
- R. Katoh, M. Kurata, and J. Yoshida, "A Self-Consistent Particle Simulation for (AlGa)As/GaAs HBTs with Improved Base-Collector Structures," Proceedings of the 1987 IEEE International Electron Devices Meeting, Washington, DC, 1987, pp. 248-251.
- E. Sangiorgi, M. R. Pinto, F. Venturi, and W. Fichtner, "A Hot-Carrier Analysis of Submicrometer MOSFET's," *IEEE Electron Device Lett.* 9, No. 1, 13–16 (1988).
- M. Tomizawa, K. Yokoyama, and A. Yoshii, "Nonstationary Carrier Dynamics in Quarter-Micron Si MOSFET's," *IEEE Trans. Computer-Aided Design* 7, No. 2, 254–258 (1988).
- K. Tomizawa and H. Hashizume, "Ensemble Monte Carlo Simulation of an AlGaAs/GaAs Heterostructure MIS-Like FET," IEEE Trans. Electron Devices 35, No. 7, 849-856 (1988).
- K. Kato, "Hot-Carrier Simulation of MOSFET's Using a High-Speed Monte Carlo Method," *IEEE Trans. Electron Devices* 35, No. 8, 1344–1350 (1988).
- D. Y. Cheng, K. Wu, C. G. Hwang, and R. W. Dutton, "Drain Contact Boundary Specification in Windowed Monte-Carlo Device with Different Collector Designs," *IEEE Electron Device* Lett. 9, No. 10, 503–505 (1988).
- J. Hu, K. Tomizawa, and D. Pavlidis, "Monte Carlo Approach to Transient Analysis of HBT's with Different Collector Designs," *IEEE Electron Device Lett.* 10, No. 2, 55-57 (1989).
- T. L. Crandle, J. R. East, and P. A. Blakey, "Monte Carlo Modeling of Electron Transport in Repeated Overshoot Structures," *IEEE Trans. Electron Devices* 36, No. 2, 300–308 (1989).

- 60. The Roman orator, Cicero, told the story of Damocles, a courtier of the Greek tyrant Dionysius of Syracuse. In the story, Damocles talked so often of Dionysius' happiness that the tyrant decided to teach him a lesson. He invited Damocles to sit at the tyrant's own place at the banquet. Damocles was horrified to find a sword suspended by a single hair above his head. Dionysius thus demonstrated to him the precarious nature of positions of power, even when apparently secure.
- M. V. Fischetti and S. E. Laux, "Monte Carlo Analysis of Electron Transport in Small Semiconductor Devices Including Band-Structure and Space-Charge Effects," *Phys. Rev. B* 38, No. 14, 9721–9745 (1988).
- S. E. Laux and M. V. Fischetti, "Monte-Carlo Simulation of Submicrometer Si n-MOSFET's at 77 and 300 K," *IEEE Electron Device Lett.* 9, No. 9, 467–469 (1988).
- M. V. Fischetti and S. E. Laux, "Monte Carlo Simulation of Submicron Si MOSFETs," Simulation of Semiconductor Devices and Processes, Vol. 3, G. Baccarani and M. Rudan, Eds., Technoprint, Bologna, Italy, 1988, pp. 349–368.
- M. L. Cohen and T. K. Bergstresser, "Band Structures and Pseudopotential Form Factors for Fourteen Semiconductors of the Diamond and Zinc-Blend Structures," *Phys. Rev.* 141, No. 2, 789-796 (1966).
- G. Ottaviani, L. Reggiani, C. Canali, F. Nava, and A. Alberigi-Quaranta, "Hole Drift Velocity in Silicon," *Phys. Rev. B* 12, No. 8, 3318–3329 (1975).
- W. N. Grant, "Electron and Hole Ionization Rates in Epitaxial Silicon at High Electric Fields," Solid State Electron. 16, No. 10, 1189–1203 (1973).
- C. A. Lee, R. A. Logan, R. L. Batdorf, J. J. Kleimack, and W. Wiegmann, "Ionization Rates of Holes and Electrons in Silicon," *Phys. Rev. A* 134, No. 3, 761-773 (1964).
- L. D. Landau and E. M. Lifshitz, Statistical Physics, Addison-Wesley Publishing Co., Reading, MA, 1969, p. 149.
- R. E. Bank and D. J. Rose, "Parameter Selection for Newton-Like Methods Applicable to Nonlinear Partial Differential Equations," SIAM J. Numer. Anal. 17, No. 6, 806–822 (1980).
- A. Phillips, Jr. and P. J. Price, "Monte Carlo Calculations on Hot Electron Energy Tails," Appl. Phys. Lett. 30, No. 10, 528– 530 (1977).
- E. Sangiorgi, B. Riccó, and F. Venturi, "MOS²: An Efficient Monte Carlo Simulator for MOS Devices," *IEEE Trans. Computer-Aided Design* 7, No. 2, 259–271 (1988).
- G. A. Sai-Halasz, M. R. Wordeman, D. P. Kern, S. Rishton, and E. Ganin, "High Transconductance and Velocity Overshoot in NMOS Devices at the 0.1-μm Gate-Length Level," *IEEE* Electron Device Lett. 9, No. 9, 464–466 (1988).
- G. A. Sai-Halasz, M. R. Wordeman, D. P. Kern, S. A. Rishton, E. Ganin, T. H. P. Chang, and R. H. Dennard, "Experimental Technology and Performance of 0.1-μm-Gate-Length FETs Operated at Liquid-Nitrogen Temperature," *IBM J. Res.* Develop. 34, No. 4, 452–465 (1990, this issue).
- 75. Personal communication, P. J. Price, IBM Thomas J. Watson Research Center, Yorktown Heights, NY, March 1989.
- C. Kittel, Quantum Theory of Solids, John Wiley & Sons, Inc., New York, 1963, p. 88.
- Personal communication, P. Lazzareschi, IBM Thomas J. Watson Research Center, Yorktown Heights, NY, December 1988

Received April 19, 1989; accepted for publication October 27, 1989

Steven E. Laux IBM Research Division, Thomas J. Watson Research Center, P.O. Box 218, Yorktown Heights, New York 10598. Dr. Laux received his B.S. degree in electrical engineering from Purdue University in 1976. He received his M.S.E. and Ph.D. degrees, both in electrical engineering, from the University of Michigan in 1977 and 1981, respectively. He subsequently joined IBM at the Thomas J. Watson Research Center, initially to work on silicon devices. Dr. Laux is currently a Research Staff Member in the Logic, Memory and Packaging Department, working on semiconductor device modeling. His interests include semiconductor physics and modeling, large-scale computing, and applied mathematics. In 1989 he received an IBM Outstanding Innovation Award for the creation of the DAMOCLES program. Dr. Laux is a senior member of the Institute of Electrical and Electronics Engineers.

Massimo V. Fischetti IBM Research Division, Thomas J. Watson Research Center, P.O. Box 218, Yorktown Heights, New York 10598. Dr. Fischetti graduated from the University of Milan, Italy, in 1974 with a "Laurea" in physics. He received a Ph.D. degree in physics from the University of California, Santa Barbara, in 1978. Dr. Fischetti joined the Thomas J. Watson Research Center in 1983, after four years of experience in experimental solid-state physics at the Physics Laboratories of SGS-Thomson and 3M-Italy. He is currently a Research Staff Member in the Logic, Memory and Packaging Department, Dr. Fischetti has done experimental and theoretical work on the degradation of thin silicon dioxide films and on the theory of electron transport in insulators. He has received two IBM Outstanding Innovation Awards: one in 1986 for the Monte Carlo simulation of electron transport in SiO₂, and one in 1989 for the creation of the DAMOCLES program, Since 1985, Dr. Fischetti has been working on the Monte Carlo modeling of electron transport in small semiconductor devices.

David J. Frank IBM Research Division, Thomas J. Watson Research Center, P.O. Box 218, Yorktown Heights, New York 10598. Dr. Frank received a B.S. degree from the California Institute of Technology in 1977, and a Ph.D. degree in physics from Harvard University in 1983. Since then he has been employed at the Thomas J. Watson Research Center, initially as a Postdoctoral Fellow in the Physical Sciences Department, studying nonequilibrium superconductivity, and currently as a Research Staff Member in the Logic, Memory and Packaging Department, modeling III–V devices. His interests include superconductor and semiconductor device physics, modeling and measurement, circuit design, and percolation in two-dimensional systems. Dr. Frank is a member of the American Physical Society.